Nanoscale

Magnetic and Dielectric Property Control in the Multivalent Nanoscale Perovskite $Eu_{0.5}Ba_{0.5}TiO_3$

Journal:	*Nanoscale*
Manuscript ID	NR-ART-01-2021-000588.R1
Article Type:	Paper
Date Submitted by the Author:	30-Apr-2021
Complete List of Authors:	Farahmand, Nasim; The Graduate Center of the City University of New York, Ph.D. Program in Chemistry; McGinn, CK; Columbia University, Zhang, Qize; CUNY The Graduate Center, PhD Program in Chemistry Gai, Zheng; Oak Ridge National Laboratory, CNMS Kymissis, Ioannis; Columbia University, Department of Electrical Engineering O'Brien, Stephen; City College of New York, Chemistry

Magnetic and Dielectric Property Control in the Multivalent Nanoscale Perovskite $Eu_{0.5}Ba_{0.5}TiO_3$

Nasim Farahmand[a,b,c], Christine K. McGinn[d], Qize Zhang[b,c,e], Zheng Gai[f], Ioannis Kymissis[d] and Stephen O'Brien[a,b,c*]

[a] The CUNY Energy Institute, City University of New York, Steinman Hall, 160 Convent Avenue, The City College of New York, New York, NY 10031, USA.

[b] Department of Chemistry, The City College of New York, 1024 Marshak, 160 Convent Avenue, NY 10031, USA

[c] Ph.D. Program in Chemistry, The Graduate Center of the City University of New York, New York, NY 10016, USA.

[d] Department of Electrical Engineering, Columbia University, New York, New York 10027, USA

[e] Department of Radiology, Memorial Sloan Kettering Cancer Center, New York, NY 10065, USA.

[f] Center for Nanophase Materials Sciences and Chemical Science Division, Oak Ridge National Laboratory, Oak Ridge, TN 37831, USA

Keywords: nanoscale, magnetic, dielectric

ABSTRACT

We report nanoscale $Eu_{0.5}Ba_{0.5}TiO_3$, a multiferroic in the bulk and candidate in the search to quantify the electric dipole moment of the electron. $Eu_{0.5}Ba_{0.5}TiO_3$, in the form of nanoparticles and other nanostructures is interesting for nanocomposites integration, biomedical imaging and fundamental research, based upon the prospect of polarizability, *f*-orbital magnetism and tunable optical/radio luminescence. We developed a [non-hydrolytic]sol–[H_2O-activated]gel route, derived from in-house metallic $Ba_{(s)}/Eu_{(s)}$ alkoxide precursors and $Ti\{(OCH(CH_3)_2\}_4$. Two distinct nanoscale compounds of Ba:Ti:Eu with the parent perovskite crystal structure were produced, with variable dielectric, magnetic and optical properties, based on altering the oxidizing/reducing conditions. $Eu_{0.5}Ba_{0.5}TiO_3$ prepared under Air/O_2 atmospheres produced a spherical core-shell nanostructure (30-35 nm), with perovskite $Eu_{0.5}Ba_{0.5}TiO_3$ nanocrystal core-insulating oxide shell layer (~3 nm), presumed a pre-pyrochlore layer abundant with Eu^{3+}. Fluorescence spectroscopy shows a high intensity $^5D_0 \rightarrow {}^7F_2$ transition at 622 nm and strong red fluorescence. The core/shell structure demonstrated excellent capacitive properties: assembly into dielectric thin films gave low conductivity (2133 GΩ/mm) and an extremely stable, low loss permittivity of ε_{eff} ~25 over a wide frequency range (tan δ < 0.01, 100 kHz - 2 MHz). $Eu_{0.5}Ba_{0.5}TiO_3$ prepared under H_2/Argon produced more irregular shaped nanocrystals (20-25) nm, with a thin film permittivity around 4 times greater (ε_{eff} 101, tan δ <0.05, 10 KHz-2 MHz, σ ~59.54 kΩ/mm). Field-cooled Magnetization values of 0.025 emu/g for EBTO-Air and 0.84 emu/g for EBTO-Argon were observed. X-ray photoelectron spectroscopy analysis reveals a complex interplay of $Eu^{II/III}/Ti^{III/IV}$ configurations which contribute to the observed ferroic and fluorescence behavior.

INTRODUCTION

In recent years, $EuTiO_3$ (ETO) and certain substituted analogues, such as $Eu_{0.5}Ba_{0.5}TiO_3$ (EBTO) have come into focus, due to potential magnetoelectric applications[1,2] together with fundamental interest in the search for the electric-dipole moment of the electron.[3–5] The Eu-Ba-Ti-O system presents potential for large dielectric polarization and ferroelectricity, combined with spin configurations that give rise to ferromagnetic order and emergent phenomena.[6] ETO, [2,7,8] a G-type

antiferromagnetic below T_N (5.2K),[2] adopts the cubic perovskite structure at room temperature, undergoing a structural phase transition to tetragonal at 282K. A large magnetoelectric coupling has been reported: alongside a dielectric constant that increases with decreasing temperature but drops dramatically at T_N.[9,10] The search for the permanent electric dipole moment (EDM) is motivated by the Standard Model, in which a known issue, that of charge-conjugation/parity (CP) violation, is theoretically supposed to exist in order to support matter-antimatter asymmetry, but proves hard to detect. The matter-antimatter asymmetry problem, also called Baryon asymmetry, is fundamental to physical cosmology as it attempts to address the observed imbalance in baryonic matter (the type of matter experienced in everyday life) and antimatter in the observable universe, for which neither the standard model of particle physics, nor the theory of general relativity can provide an explanation.[11] A promising means of EDM detection is based upon electric- field-correlated magnetization measurements in solids, in which the orientation of the magnetization is reversed when the electric field direction is switched, and could be detected by a SQUID magnetometer.[10] The experiment aims to detect the intrinsic magnetoelectric response associated with the minute EDM of the electron, causing the design constraints to be stringent. $Eu_{0.5}Ba_{0.5}TiO_3$ is contemplated for EDM research, since the desired material should be ferroelectric, possess a large dielectric polarization, and have a high concentration of heavy ions with local magnetic moments (proportional to Z^3). The Eu^{2+} ion has seven unpaired localized 4f electrons, resulting in a large spin magnetization of 7μB, and a large mean displacement of the Eu^{2+} ion with respect to oxygen (0.01 Å) that contributes to a ~1 μCcm^{-2} remanent polarization to create a large electric field response.[2,10] Such stringent criteria critically limit the range of available materials, hence the focus on this rather unique and interesting compound.[3]

Magnetoelectric (ME) coupling is the enactment of a magnetic field (M) on an electric field (E) or vice versa, and may exist in either a single phase material or in composites. Furthermore, ME coupling can occur across different order parameters, for example between paramagnetic and ferroelectric.[12] ME coupling is described in (Landau) terms of polarization $P_i(H_j)$ or magnetization $M_i(E_j)$, for with a linear magnetic coupling coefficient , $\alpha_{ij}{}^2 \leq \varepsilon_0\varepsilon_{ij}\mu_0\mu_{ij}$, where ε_0, ε_{ij} and μ_0, μ_{ij} are the free space and relative permittivities and permeabilities respectively. Determining material values of ε and μ are very important. Coupling in composites is often via an indirect magnetostrictive effect, in which change of shape or dimension from magnetization can induce a change in polarization. Nanoparticle-polymer 0-3 composites can deliver magnetostriction, hence

nanoparticles are very interesting in this context.[13] True ME coupling within a single phase is rare, much debated and highly sought,[4,14–16] Europium barium titanate, EBTO, presents a compelling case for study in the context of multiferroic complex oxides,[17] since it's bulk behavior is both ferromagnetic/ferroelectric, and has notable values of μ_{ij} and ε_{ij} with prospect for a high ${\alpha_{ij}}^2$. Janes *et al.* originally reported magnetization values of 59 emu g^{-1} (1.8 K, 5 kOe), a Curie temperature of 165 K and a saturation polarization of 9.5 μC/cm^2 (15.7 kV/cm, 35 Hz).[18] More recently, sintered ceramics of (Ba,Eu)TiO_3, with 60% density, intended for EDM research were reported by Sushkov *et al.* with high permittivity, a saturation polarization of 8.0 μC/cm^2 (remanent polarization P_r = 1 μC/cm^2), and no magnetic hysteresis and magnetic susceptibility χ values in the range 0.01-0.06 emu g^{-1} Oe^{-1} (< 4K).[3,10]

While some bulk synthesis methods of $Eu_{0.5}Ba_{0.5}TiO_3$ have been researched, preparing nanoscale synthetic analogues remain largely unexplored. The nanoscale offers the potential to control properties when compared to the corresponding bulk material, due to strong interplay between elastic, geometric and electronic parameters. While suppression of ferroic order parameters is observed in perovskites at the nanoscale, there is strong evidence to support the retention of off-center Ti distortions down to 5 nm, that can be the source of switchable dipoles, and ultimately ferroelectricity.[19–22] concurrently, the field of nanomagnetism has flourished, due in part to the increasing sensitivity of the techniques developed for magnetic property-structure relationships.[23] Our interest in $Eu_{0.5}Ba_{0.5}TiO_3$ extended to: (i) obtaining a multiferroic with metastable phases unique to the nanoscale; (ii) measuring and controlling size dependent properties; and (iii) utilizing nanoscale $Eu_{0.5}Ba_{0.5}TiO_3$ as building blocks for hierarchically assembled structures or ferroic nanocomposites.[24] The opportunity to isolate metastable phases through nanoscale processing is quite profound.[25] It is particularly important to recognize the relationship between product stabilization and thermodynamic pathway, as determined by the starting reactants,[26] observing that the molecular precursor based reactions can lead to scaffolding of initial phases or structural motifs, which can have an exacting influence over the final product structure, provided crystallization temperatures are kept below thermodynamic limits for the bulk phase diagram. The synthetic pathway chosen here was partly motivated by previous observations that when perovskite $EuTiO_3$ is heated in air, it is metastable, forming an amorphous perovskite-related intermediate present around 500°C. At 750°C, a layered perovskite polymorph of $Eu_2Ti_2O_7$ begins to crystallize

but this too is metastable until conversion to the pyrochlore $Eu_2Ti_2O_7$ polymorph from 900 °C onwards.[27] The addition of barium to the lattice via precursor synthesis was predicted to stabilize the cubic perovskite structure, providing alternate vectors for the metastable phases.

The interconversion between Eu(II) and Eu(III) can influence structure and properties, including multiferroic behavior. Therefore, understanding how to chemically stabilize Eu(II) and/or Eu(III) within the perovskite structure is of interest. Research into dilute/doping concentrations of Eu^{3+}/Eu^{2+} incorporated $BaTiO_3$ have been reported,[28,29] but structures in which Eu is a dominant element with direct influence over phase stability are less well understood. Recently, research has shown that controlling oxygen deficiency through $Ti^{3+}/3d^1$ creation in $(Eu,Ba)TiO_3$ can influence multiferroic behavior.[30] But, it has also become apparent that several assumptions regarding the stoichiometry, oxidation state, and phase of Eu-based perovskite compounds require further investigation, especially when regarding the relative concentrations of Eu^{2+} and Eu^{3+}. The standard partial molar Gibbs free energy of formation are quite close at room temperature: $\Delta G_f^\circ(Eu^{2+})$ = 540.2 kJmol^{-1}; $\Delta G_f^\circ(Eu^{3+})$ = 574.0 kJmol^{-1}, the redox potential Eu^{3+}/Eu^{2+}, E° = -0.35V. At elevated temperatures and pressures (including hydrothermal conditions), the divalent state becomes more stable, helping to explain the presence of Eu^{2+} in barite.[31] Luminescence data highlights how the electronic configuration for Eu^{3+}, $4f^6$, is chemically very stable,[32] although Eu^{2+}, while thought to be metastable,[33] is often present. In Eu^{3+}, *f–f* electron transitions are shielded by the completely filled external 5s/5p orbitals. The Eu^{2+} electron configuration ($4f^7$) is less localized and exhibits stronger phonon coupling. This leads to an *f-d* transition subject to the influence of temperature dependent vibrations of the host lattice, coordination and symmetry.[32] It is additionally noted therefore, Eu^{2+} in the A site of $(Eu,Ba)TiO_3$, while presumed geometrically suitable, may be chemically labile.[34] The band-width and relative intensity of the photoluminescence (PL) spectra depends on the crystal symmetry of the host.[35]

To prepare nanoscale $Eu_{0.5}Ba_{0.5}TiO_3$, we relied on a modified sol-gel approach which has proven successful for room temperature synthesis of oxide perovskite nanocrystals.[36,37] Our previous observations of $Ti(^iOPr)_4$ driven perovskite formation, combined with Ba^{2+} stabilization of the lattice suggested the ability to stabilize Eu in the cubic structure in the absence of Ar/H_2, which we pursued. This chemical solution processing method (gel-collection), developed for the preparation of inorganic oxide nanomaterials and films, has been reported in detail previously.[38–40] More general motivation is that low temperature chemical methods may prove to be low-cost

and easy to integrate within existing manufacturing frameworks, or prove compatible with a disruptive approach like r2r fabrication,[41] and R&D efforts can take advantage of low temperature techniques toward materials discovery.[42,43]

The combination of $BaTiO_3$ and $EuTiO_3$ presents an interesting set of structure-property outcomes: both $EuTiO_3$ and $BaTiO_3$ have ABO_3 perovskite structure with Eu^{2+} and Ba^{2+} on the A site and Ti^{4+} on the B site.[10] $BaTiO_3$ is a prototypical ferroelectric with a large room-temperature polarization of 25 μCcm^{-2}. $EuTiO_3$ is reported to be a quantum paraelectric with a large dielectric constant (ε ~400),[9,44] while electronic structure calculations show that ferroelectricity could be induced from elongation (compressive or tensile strain)[45]. Synthesis methods for (Eu,Ba)TiO_3 compounds have previously included ceramic solid state reactions[3,46–49], hydrothermal,[50] vapor diffusion,[28] PLD,[30] and high temperature mechanochemical activation.[10] Materials engineering of nanoscale Eu-Ba-Ti-O could be attempted via bulk solid state processing and ball-milling, but this presents drawbacks in terms of product fidelity and size control. Through an approach more akin to molecular templating to drive crystallization, at lower temperatures and under variable redox conditions, we attempted to realize the goal of controlling phase and oxidation state, based on modified sol-gel chemistry techniques used by our group and others.[36,51–53]

EXPERIMENTAL

Synthesis. 6.5 wt% barium ethoxide ($Ba(OCH_2CH_3)_2$ was prepared in the lab by dissolving barium metal pieces in pure ethanol (200 proof) after stirring magnetically overnight in nitrogen glovebox. Barium metal pieces were purchased from Alfa Aesar, and pure ethanol (200 proof) purchased from Decon Laboratories, Inc., titanium isopropoxide ($Ti\{(OCH(CH_3)_2\}_4$) and europium metal pieces were purchased from Sigma-Aldrich and Alfa Aesar respectively. All elements/chemicals were used as purchased. The EBTO nanoparticles were synthesized using the gel collection method[36] under an inert nitrogen atmosphere in glovebox. In order to make $Eu_{0.5}Ba_{0.5}TiO_3$, stoichiometric amounts of europium metal (0.473 g or 3.125 mmol) was dissolved in 40 mL of 200 pure ethanol and magnetically stirred until the metal pieces dissolved and the colorless solution started to gain color. A dark brown solution was obtained after staying overnight in the glovebox and then centrifuged for 15 min, 6500 rpm to form a clear yellow solution. This solution was presumed to be $Eu(OCH_2CH_3)_2$.[54] Stoichiometric amounts of lab-made barium ethoxide (3.125 mmol or 6.60 mL) was added to the europium solution and stirred

magnetically for 20 minutes. Then 1.89 mL of $Ti\{(OCH(CH_3)_2\}_4$) was added and the solution immediately turned black upon addition of titanium isopropoxide. The absence of water at this stage prevents the premature self-hydrolysis of the molecular precursors. After another 20 minutes of stirring, a 10 mL solution of 2.5 mL deionized H_2O (4% DI water of total volume) and 7.5 mL 200 proof ethanol was prepared and added dropwise to the solution under stirring leading to form a black gel. The gel was transferred to a sealed container (e.g. a centrifuge tube with a cap) and left to age overnight in the glovebox. Once formed, the gel was readily extracted from the mother solution (ethanol) and could be removed, divided into parts and thermally treated for crystallization. Portions of the gel were treated in two ways: (i) 650°C (1°C/min) for 8 hours both in air (upright furnace) and (ii) under Argon/Hydrogen Ar (95%)/H_2(5%). For Ar/H_2, a sealed tube furnace with bubbler, connected to the Ar/H_2 tank was used. The resulting Europium Barium Titanate (EBTO) nanoparticles were characterized using powder X-ray diffraction (XRD), X-ray Photoelectron Spectroscopy (XPS), Transmission Electron Microscopy(TEM) and Energy Dispersive X-ray Spectroscopy (EDS). The XRD measurements of the dried EBTO powder were performed on a PANalytical X' Pert Pro using Cu Kα radiation. XPS measurements were recorded on the EBTO powder samples on a Physical Electronics Versaprobe II XPS. The XPS peaks were fitted using Multipak v. 9.6.0.15 software. TEM was performed using a JEOL 2100. Samples for the TEM were prepared by dispersing the nanocrystalline powders in 200 proof ethanol and drop-casting 5μL of the resulting suspension on a carbon coated copper grid. TEM and EDS measurements were recorded on a JEOL 2100 microscope. Diffuse reflectance (DR) spectra were obtained from UV to NIR (200-800 nm) using a CARY 500 spectrophotometer equipped with a diffuse reflectance accessory (integrating sphere). Room temperature photoluminescence (PL) emission spectra of the samples (230 nm excitation) were collected using Spectramax id5 instrument (Molecular Devices).

The voltage tolerance and resistance of the EBTO-Air and EBTO-Argon samples was characterized using a Keithley 2440 source meter. For EBTO-Air, the voltage range used was 0V to 200V with steps of 4V. For EBTO-Ar, the voltage range used was 0V to 10V with steps of 0.4V. At each voltage, the current observed by the Keithley was recorded. The resistivity was calculated using the equation $\rho = A/(m*L)$, where m is the slope of the linear I-V curve, A is the area of the sample, and L is the thickness of the pellet. The area and thickness of the samples respectively were 1 cm^2 and 0.1mm thick. To determine the voltage tolerance, each I-V curve

was fitted linearly and the voltage tolerance was extrapolated as the point where the current density crosses 10 μA/cm^2.

Results and Discussion

Gel collection[36] was applied to synthesize europium barium titanate and resulted in highly crystalline, single phase perovskite crystal structures of the form $Eu_{0.5}Ba_{0.5}TiO_3$, (referred to in this article as EBTO), with the observation of the formation of multivalent versions dependent on processing conditions. One initial concern, with a major influence over electronic/magnetic properties, is determining whether lanthanide ions in ABO_3 occupies a single site (Ba or Ti) or multiple sites (Ba and Ti). The Shannon ionic radius for Eu^{2+} (Z=63) ranges from 117 pm (C.N. 6) to 135 pm (C.N. 10), while the ionic radius of Eu^{3+} ranges from 95 pm (C.N. 6) to 112 pm (C.N. 9). For $BaTiO_3$ the ionic radii are assumed to be Ba^{2+} (Z=56), 161 pm (C.N. 12), and Ti^{4+} (Z=22) 61 pm (C.N. 6). The Shannon ionic radius of Ti^{3+} is reported to be 67 pm (C.N. 6). Europium is not typically observed to adopt a 12-fold coordination, and is nearly three times the atomic number of titanium. In terms of europium as a fit for the ABO_3 system, the Eu^{2+} cation size appears to present little problem (compare Ca^{2+}, 135 pm (C.N. 12)). Shannon et al.[55] predicts that when Eu^{3+} replaces Ti^{4+} in the structure, the crystal lattice expands. The Goldschmidt tolerance factor (t) for $BaTiO_3$, is t = 1.06. For $Eu_{0.5}Ba_{0.5}TiO_3$ with Eu^{2+} in the A site: t = 1.01; with a mixture of 50% Eu^{3+}/Eu^{2+} (neglecting the implication of charge): t = 0.98 (see Supplementary Information). Since the radius of the Eu^{3+} ion is intermediate between the radius of the Ba^{2+} and Ti^{4+}, it could potentially occupy either the A site or B site depending on Ba/Ti ratio.[28,56] Generally, it has been reported that the larger ions occupy the Ba^{2+} site predominantly and present donor behavior, while smaller ions prefer the B site and exhibit acceptor behavior.[57] Fang *et al*,[58] and Fuentes *et al.*[59] reported Eu^{3+} can be substituted into both Ba^{2+} cation and Ti^{4+} ion sites, with some lattice distortion. A second, related concern is regarding oxidation state of the lanthanide. This is especially relevant in the case of Eu, for which presupposing Eu in the perovskite is solely Eu^{2+} (as if it were replacing Ba^{2+}), and that Ti would be solely Ti^{4+}, may not be judicious., since the ionic model is less appropriate for strongly correlated oxides. The classical model for titanium in ABO_3 is with an oxidation state of IV, but there are cases for which Ti is either solely or partially (III). For example, while maintaining near perfect integrity

of the perovskite atomic arrangement, Jang *et al.* reported the ability to create RO line defects (R=La, Sm, Nd) in between $SrTiO_3$, for which Ti is formally in the 3+ oxidation state.[60] $YTiO_3$ is a spin-ordered ferromagnetic d^1 orthorhombic perovskite (space group *Pbnm*) for which the presence of the Ti^{III}/d^1 state accounts the majority of its properties.[61] Fujimori *et al.* considered a series of d^1 transition metal oxides on the basis of a singleband Hubbard model, and explained the opening of the band gap, from metallic VO_2 to insulating $YTiO_3/LaTiO_3$.[62] The contrast of early and late transition metals can be characterized by firm differences in the electron correlation effects and extent of orbital mixing. Early transition metal compounds, containing Ti are characterized by a large extent of *p-d* orbital hybridization ($pd\sigma$), and a concurrent strong covalency, found to increase as the number of d-electrons decreases. While $YTiO_3$ and $LaTiO_3$ are d^1 ($t_{2g}^1e_g^0$) compounds with a formal valence of 3+, a lower oxidation state is calculated, with n_d estimated to be 1.8/1.9, where n_d = net d-electron occupancy.[62] Treating $Eu_{0.5}Ba_{0.5}TiO_3$ as an orbitally mixed compound, as opposed to an ionic ceramic, is therefore considered appropriate.

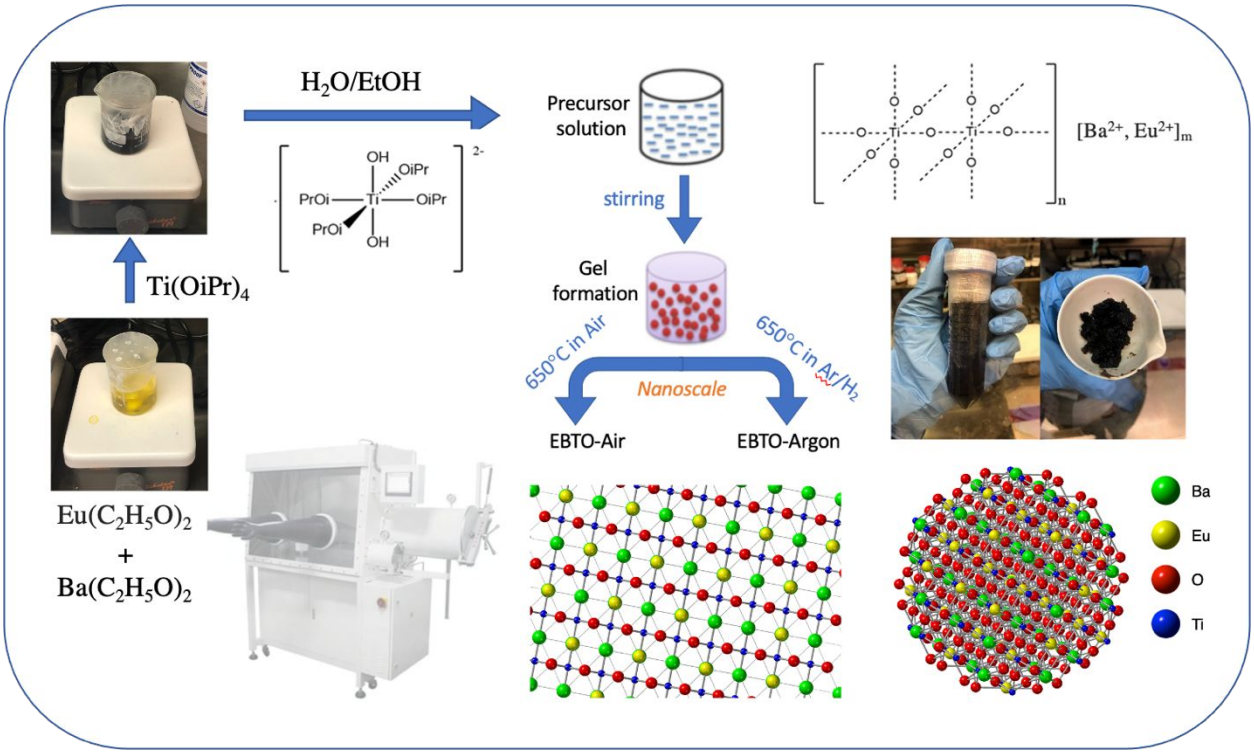

Fig. 1. Schematic for synthesis and crystal structure of nanoscale $Eu_{0.5}Ba_{0.5}TiO_3$.

Applying gel-collection as the synthesis method at room temperature allowed the preparation of amorphous nanoparticles of Eu-Ba-Ti-O, and thermal treatment at 650°C was

necessary to complete crystallization (see Fig. 1). The in-house prepared precursors of ($Ba(OCH_2CH_3)_2$ and purchased ($Ti\{(OCH(CH_3)_2\}_4$), $Ti(^iOPr)_4$, reacted as anticipated. The in-house prepared precursor for europium "dissolution" ethanol was assumed to be $Eu(OCH_2CH_3)_2$, with divalent europium, according to previously reported Mossbauer spectroscopic characterization.[54] We can posit the mechanism, in the absence of water, is that loosely bound transition metal oxide species of $Ba(OR)_2$ and $Eu(OR)_2$ form a homogenous mixture. The addition of $Ti(^iOPr)_4$ to the mixture prompts a nucleophilic addition reaction as the $M(OR)_2$ molecules insert between $Ti(^iOPr)_4$, forming chains and commencing oxolation - the formation of bridging oxygen between metal centers.[63] With the addition of H_2O, a more vigorous hydrolysis is initiated, involving the formation of *oxo*-bridging groups and CH_3CH_2OH and $HOCH(CH_3)_2$ as leaving groups. The premixing and homogenization of the metal centers, paves the way for the formation of chains (becoming a corner sharing network) of TiO_6 octahedra amidst a charge balanced configuration of Ba/Eu ions. Alkoxy groups still remain within the framework without complete condensation having occurred. At room temperature, the sol that has been generated remains largely amorphous to powder XRD detection limits. The sol is composed of relatively uniform nanoparticulates that can be isolated as a gel for further processing - the gel is itself a solid object composed of a loose aggregation of nanoparticles (a particulate gel monolith). Nanoscale crystallization at lower temperatures can then occur without sintering. At 650°C, crystallization of the nanoparticle occurs through the process of framework condensation, via thermal dihydroxylation and dealkoxylation. Viscous sintering, and ceramic densification, driven by the energy gained in reduction in surface area, is not observed at 650°C: temperatures for sintering transition metal oxides are typically 1100-1300°C, approximately twice that of the nanoparticulate crystallization temperature used here.

Following reaction of the precursors and isolation of the black gel monolith, the gel was divided into two parts, for either thermal treatment (650°C) in air/O_2, or Argon/Hydrogen (95% Ar:5% H_2), an oxidizing or reducing environment respectively. These two pathways were chosen to investigate stability/metastability of the nanoscale (Ba, Eu)TiO_3 oxide under these conditions. As reported previously, bulk $EuTiO_3$ reverts to the pyrcholore polymorph above 900 °C,[27] whereas it was hypothesized that introduction of Ba into the structure would favor stabilization of the cubic perovskite framework,[3] even under ambient/air thermal treatment conditions. The products formed can be described as a nanocrystalline powder in which free nanoparticles in the

size range 20-40 nm are loosely aggregated. Sizeable batch quantities (> 500mg) are readily produced. Sonication in ethanol produces a nanoparticle powder dispersion (Fig. 1). While differently processed samples shared the same perovskite structure, there were very strong observable differences in their physical properties, including color, magnetic properties, and frequency dependent dielectric behavior. The sample sets are referred to as EBTO – Europium Barium Titanium Oxide, with the affix EBTO-Air (prepared in air) or EBTO-Argon (prepared in Argon/H_2).

1. Physical/Structural Characterization

Powder X-ray diffraction shows the perovskite EBTO structures for both samples in air and in reducing atmosphere, labeled with peak positions and identifiable Bragg planes. The initial gel was heat treated in air and in Ar/H_2 to a series of temperatures, starting from 450°C, 650°C, 750°C, 850°C and 1000°C (see Supporting information, Fig. S1). The samples are named EBTO-Air and EBTO-Argon. X-ray diffraction was carried out for each set of samples, both of which were amorphous at 450°C, with complete crystallization > 650°C, at which point sharp Bragg peaks of perovskite structure emerged in the XRD. The X-ray powder diffraction patterns for 650°C samples are shown in Fig. 2, together with representative electron micrographs and images of the powder samples. The first striking difference is that, in spite of very similar X-ray powder diffraction patterns and TEM images, one is black (EBTO-Ar) and one is white (EBTO-Air). Indexing of the Bragg peaks in both cases (see Fig. 2) corresponds to a phase pure perovskite. The Bragg reflections for the lattice planes in the powder diffraction spectrum of EBTO-Air are systematically shifted to smaller values by 0.2° 2θ when compared to those of EBTO-Argon. There is evidence of a slight shoulder of the (110) peak at around 28° 2θ, in both cases which can be attributed to presence of trace barium carbonate impurity occurring on exposure to ambient conditions, due to moisture absorption on the nanoparticle surface. Previous investigations of sub-10nm barium titanate nanoparticles have indicated that surface Ba^{2+} is susceptible, over time to reaction with moisture from the air to form trace quantities of $BaCO_3$.[37] To test the structural and chemical stability of nanoscale EBTO, samples were left on the bench for 4 months, under conditions of ambient temperature, pressure and atmospheric moisture. In both cases the EBTO perovskite structure was retained as determined by powder XRD, but with a slight growth of an amorphous shoulder around 28° 2θ (Supporting Information, Fig. S2). We

conclude that the same reaction with the ambient surroundings is happening in this case. The formation of trace $BaCO_3$ can also be reduced by washing the sample with D.I. water.

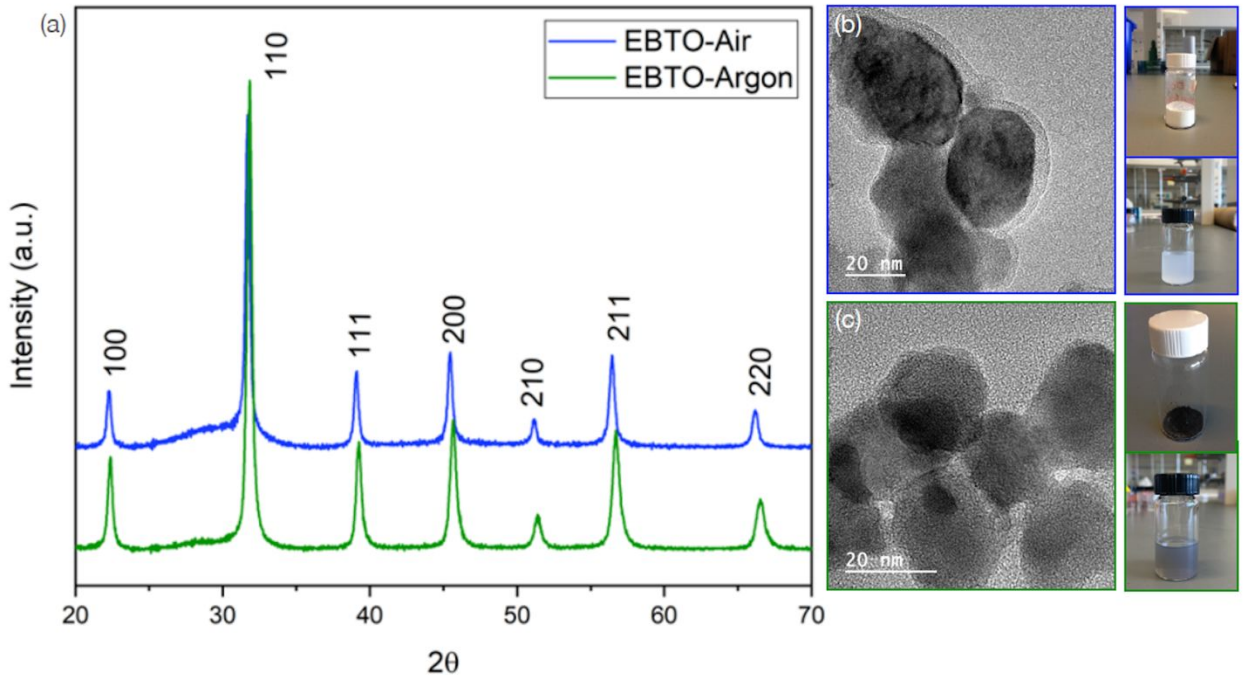

Fig. 2 a) Powder XRD and TEM images of EBTO ($Eu_{0.5}Ba_{0.5}TiO_3$), together with TEM images of (b) EBTO-Air (white) and (c) EBTO-Argon (black). Powders and ethanol dispersions also shown.

Closer analysis of the X-ray powder diffraction patterns of both samples show that the Bragg reflections for the lattice planes in the powder diffraction spectrum of EBTO-Air are shifted slightly to the left when compared to those of EBTO-Argon, corresponding to a slight difference in lattice parameter (see Supplementary Information Fig. S3). Typically, in bulk samples the FWHM of the X-ray peaks is sufficiently narrow to deduce tetragonal splitting, with focus on the (200) peak. Here the (200) FWHM is 0.46° 2θ (EBTO-Argon) and 0.38° 2θ (EBTO-Air) as a consequence of Debye-Scherrer broadening at the nanoscale. It is not possible to determine any evidence of tetragonal distortion from this data alone. Pair Distribution Function analysis (PDF) has been used previously to show strong evidence of tetragonal distortion in < 10 nm nanocrystals of perovskite $Ba(Fe,Ti)O_3$.[37] Using the Scherrer equation, the 2θ values correspond to nanoparticle sizes of 19.6 nm (Argon) and 23.7 nm (Air) respectively, in reasonable agreement with the more reliable determination of particle size by TEM. Assuming a cubic space group of $Pm\bar{3}m$ in both cases, the unit cell parameter was calculated from the Bragg reflections to be 3.99 (EBTO-Air)

and 3.97 (EBTO-Argon). This is consistent with typical cubic perovskite oxide structures, with the observation of a slightly smaller lattice constant when compared $BaTiO_3$, anticipated due to the smaller size of the $Eu^{II/III}$ cations.

The size, morphology and relative composition of the nanoparticles was further analyzed by TEM/EDS (Fig. 3). The nanoparticles disperse well in alcohols such as ethanol without the use of surfactants allowing for, among other things, EM microgrid preparation. Selected area electron diffraction indicates uniform crystallinity and that the samples are polycrystalline. Lower magnification TEM analysis and particle size distribution (Supplementary Information, Figure S4) show that the nanoparticle size distributions are in the range EBTO-Argon are in the range of 20-25 nm and for EBTO-Air is in the range of 30-35 nm. Lattice imaging further confirmed that the nanoparticles when isolated were single crystalline and presented as perovskite, with clear evidence of the (110) and (111) lattice planes in HRTEM. Electron microscopy at higher magnifications also shows a distinction between EBTO-Air and EBTO-Argon, highlighting the effect of the processing conditions. In EBTO-Air a thin amorphous layer ~2-4 nm in thickness can be observed as a shell around the crystalline core, whereas in EBTO-Argon this layer is not present. Energy dispersive X-ray spectroscopy (EDS) is capable of confirming and comparing relative amounts of high Z elements in nanocrystals. Gel-collection has previously proven reliable in terms of reactant stoichiometry being preserved in product stoichiometry.[36] For EBTO samples, EDS mapping analysis was performed in order to obtain a composition cross-section. The mapping analysis confirms the presence of Eu, Ba, Ti, O elements in the samples with fairly reliable stoichiometric ratio (for ratio table and additional TEM images see Supporting Information, Fig. S4). The shell layer in EBTO-Air is thought to be an amorphous oxide layer composed of the same elements Eu-Ba-Ti-O, based upon inferences from the EDS. This oxide layer can serve as a barrier layer, and has been known to be created synthetically in various cases including ferroic nanocomposite design.[64] In order to determine stability of the perovskite phase, and to assess whether metastable, EBTO samples were heated to 1000°C. In the case of EBTO-Argon the persistence of the perovskite phase was observed ≥1000°C (Supporting Information, Fig. S5a). However, the XRD pattern for EBTO-Air begins to reveal a mixture of phases ≥850°C (Fig. S5b). Bragg peaks that can be indexed to perovskite $(Ba,Eu)TiO_3$ and pyrochlore $Eu_2Ti_2O_7$ crystal structures emerge, alongside some smaller peaks attributed to minor europium oxide Eu_2O_3 formation - shown in detail in Fig. S6. Thermal treatment in oxygen leads to increasing amounts

of Eu^{3+}, which preferentially forms pyrochlore $Eu_2Ti_2O_7$ and some Eu_2O_3 at temperatures high enough (1000°C) for phase decomposition to occur, but at lower temperatures, preservation of perovskite the $Eu_{0.5}Ba_{0.5}TiO_3$ structure, even when heated in the presence of oxygen, is remarkably stable. This may be kinetic stability promoted by the barrier layer, which inhibits further oxidation. It is, in conclusion, interesting to observe the ability to synthesize stable nanoscale $Eu_{0.5}Ba_{0.5}TiO_3$ in oxidizing (air/O_2) as well as reducing (Argon/H_2) atmospheres.

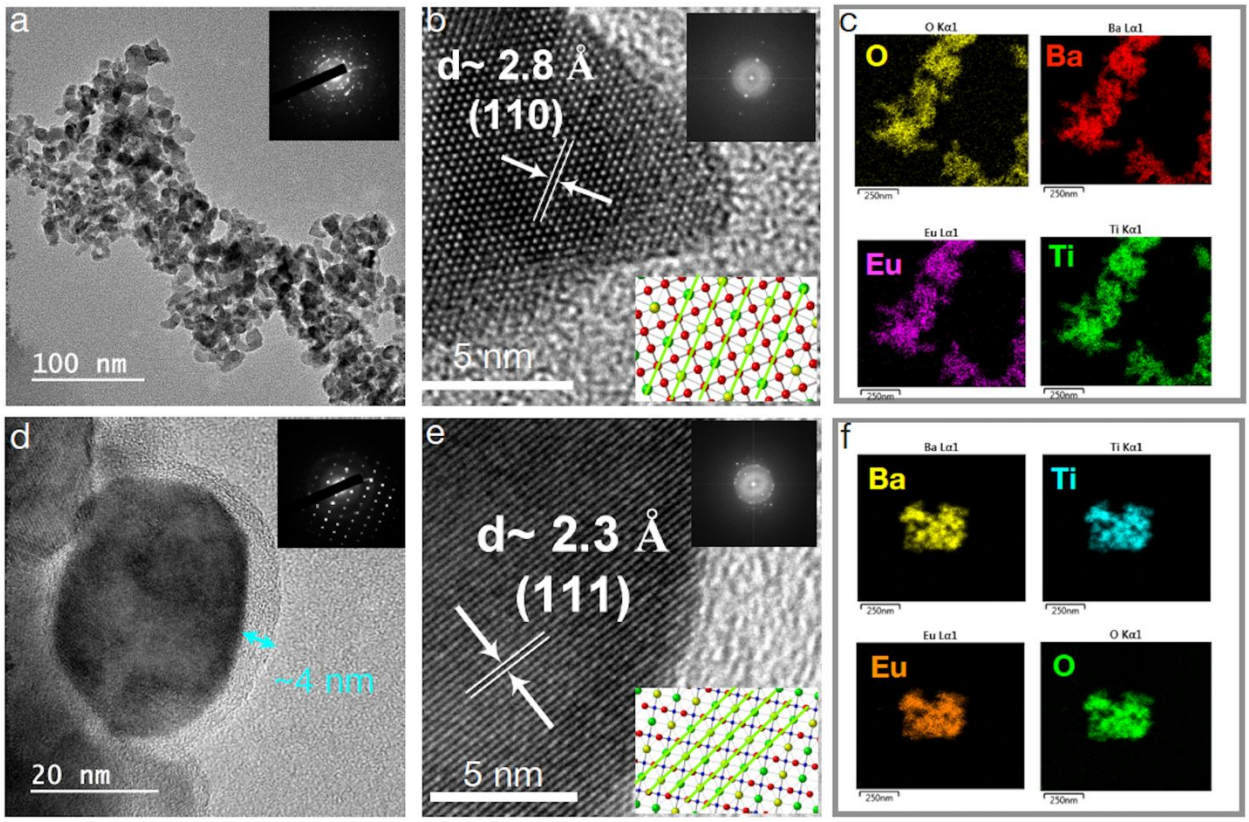

Fig. 3. TEM/HRTEM images, electron diffraction and EDS mapping of nanoscale EBTO, $Eu_{0.5}Ba_{0.5}TiO_3$: (a) TEM (b) HRTEM and (c) EDS of EBTO-Argon; (d) TEM (e) HRTEM and (f) EDS of EBTO-Air. SAED patterns also shown with crystallographic projections. EDS mapping of EBTO-Argon/Air shows the overlapping signal of Eu, Ba, Ti and O.

2. *Magnetic Characterization*

The magnetic properties of the EBTO ($Eu_{0.5}Ba_{0.5}TiO_3$) samples were analyzed in order to determine presence, extent, and type of magnetization. Magnetic measurements were performed using a Quantum Design Magnetic Property Measurement System (MPMS) at the Center for Nanophase Materials Science (CNMS) at Oak Ridge National Laboratory in Tennessee. The field cooled (FC) and zero field cooled (ZFC) measurements were carried out on EBTO samples

between the temperature range of 0-300 K. For the ZFC measurement, the samples were cooled to 5 K in the absence of an external magnetic field. Once at 5 K, an external magnetic field of 2000 Oe was applied and the magnetization was measured during the slow warming process to 300 K. For the FC measurement, the samples were cooled down to 5 K in the presence of a 2000 Oe magnetic field and the magnetization was measured during cooling under the same field. Magnetic hysteresis measurements were taken with a maximum sweeping magnetic field of 40000 Oe on the same instrument at 5 K by varying the magnetic field from -40000 Oe to 40000 Oe and measuring the magnetization. The M-H curve obtained at 5 K and 0-40000 Oe which indicates that neither of the samples reach full magnetic saturation at this magnetic field strength is shown in Fig. 4a and 4b. Zero-field cooled (ZFC) and field cooled (FC) magnetization curves (M–T) were obtained at a magnetic field of 2000 Oe, which are displayed in Fig. 4c and 4d. The highest values of magnetization observed in the FC measurement were 0.84 emu/g for EBTO-Argon and 0.025 emu/g for EBTO-Air. As the temperature is increased the magnetization decreases as a result of the randomization of the magnetic orderings within the nanoparticles due to the thermal energy. The M-T curve data allowed for the calculation of Curie and Weiss constants, using a fit to the Curie−Weiss law model according to $\chi = (C/(T-\theta) + \text{b.})$, where χ is the magnetic susceptibility (magnetization), C is the Curie constant, θ is the Weiss constant, T is the temperature in Kelvin, and b is a fitting parameter (Table 1). The Weiss constant generally allows for insight into the short-range magnetic interactions within the compound. Here, the Weiss constant values are indicative of potentially antiferromagnetic behavior which is largely obscured by paramagnetic behavior. Lack of evidence for long range antiferromagnetic ordering is attributed to the nanoscale nature of the compounds and a concurrent large number of surface spins, that contribute to spin anisotropy.[65] Comparative analysis of the M-H data at low temperatures (Figure 4(c) and 4(d)) shows clear differences by more than an order of magnitude in magnetization. Since sample particle size analysis (Figure S4) show that the nanoparticle size distributions are relatively narrow and in the range 20-25 nm for EBTO-Argon and 30-35 nm for EBTO-Air, the observable differences were attributed to composition of the two samples (particularly oxidation states of Eu) as opposed to particle size difference. HRTEM also indicated the nanoparticles are single domain in both cases. Multi-domain crystallinity would have an impact on magnetization and not observed here. As the thermal motion of the electrons is reduced, the observed overall magnetization increases proportionally to the increasing number of electrons. This can be interpreted that EBTO-

Argon sample has more unpaired electron spins, due to the reducing environment maintaining more Eu^{2+} ,$[Xe]4f^7$, compared to the EBTO-Air sample having less electrons, having been subjected to more oxidizing conditions (and therefore a higher presence of Eu^{3+}, $[Xe]4f^6$.

Table 1. Curie and Weiss constant values for EBTO-Air and EBTO-Argon samples

	Curie Constant (*C*)	Weiss Constant (*θ*)	Fitting parameter (*b*)
EBTO-Air	16.37±2.09	-524.97±41.7	-0.012±0.001
EBTO-Argon	-0.039±0.03	21.84±0.3	0.054±0.006

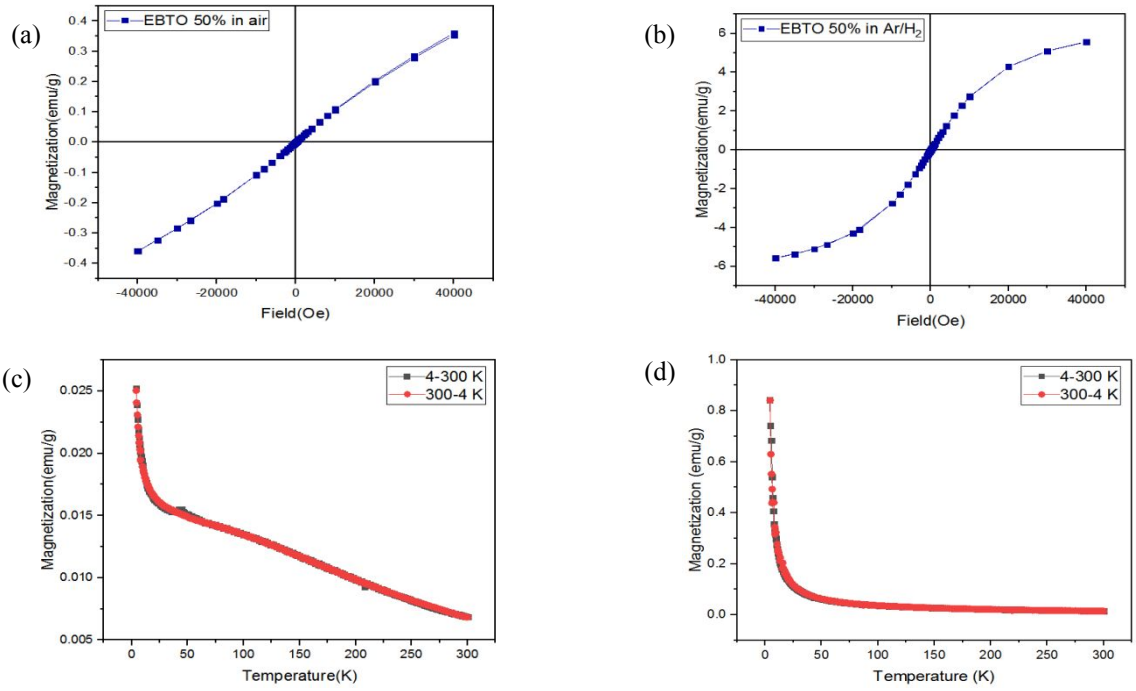

Fig. 4. a) and b) M-H curves, c and d) M-T curves for EBTO-Air and EBTO-Argon samples

3. *LCR Dielectric Measurements*

Impedance analysis was performed on the EBTO samples (Air and Argon) using an LCR meter (Inductance-Capacitance-Resistance meter) with the main goal of measuring frequency dependent permittivity. Impedance/capacitance measurement of nanoscale samples is highly dependent on the specific processing conditions of the film under measurement, due to grain size, grain surface area and void space between the grains.[66] The results can yield much information about the dielectric behavior of the compound under investigation, but the absolute value of permittivity (intrinsic dielectric constant) of nanoscale $Eu_{0.5}Ba_{0.5}TiO_3$ is more complex

to determine, requiring an air-nanoparticle composite model.[67,68] Pressed pellet capacitors of each compounds were prepared using a Cyky 12T Laboratory manual powder metallurgy press machine to provide pressed and thin round disks. The pellets were prepared as simple parallel plate capacitors using silver conductive epoxy (MG chemicals) as contacts and were kept in the furnace at 60°C overnight. LCR measurements were performed on the samples to obtain the frequency dependent effective permittivity, ε_{eff}, and dissipation loss (tan δ). Measurements were performed over the frequency range of 100 Hz to 2 MHz using an Agilent E4980A Precision LCR Meter. The frequency dependent behavior of the effective permittivity, ε_{eff}, and dissipation loss (tan δ) are shown for both samples in Fig. 5 (part a and b) and Fig. 5 (part c and d) respectively. For EBTO-Argon, the effective dielectric constant at low frequencies is ~130 (1 kHz) decreasing steadily to ~100 (1 MHz) and the dissipation loss is in the range of 0.05 shown in Fig. 5 (part a and c). In clear contrast, EBTO-Air has a very stable ε_{eff} of 25 over the entire frequency range (100 Hz-1 MHz), and shows a very low dissipation loss (~ 0.01) shown in Fig. 5 (part b and d). The EBTO-Air is concluded to perform very well as a stable dielectric material with a relatively high effective permittivity in pellet form. The frequency dependence of tan δ is shown in Fig. 5. For EBTO-Argon decreases from 0.09 (1 kHz) to 0.03 (1 MHz). This value of tan δ is quite typical of film or pellet processed nanoscale complex oxides in which low frequency loss can partly be attributed to contributing space extrinsic charge effects at the surface of the nanoparticles, while higher frequency loss is attributed to charge hopping due to the presence of multivalent metals.[40,66] The expectation of some leakage, and low to medium resistivity/dielectric strength as a result of the presence of mobile carriers is anticipated in voltage tolerance and conductivity measurements. In the case of EBTO-Air, tan δ is in the range becoming of a dielectric material 0.03 (1 kHz) to 0.007 (1 MHz), with good stability and values suitable for capacitance, energy storage applications.[69] This is interesting because, owing to the multivalent character of Eu, one would anticipate a lossier, lower resistivity film. The core-shell structure of the nanoparticle presents an interesting case for potential applications because the core retains some of the desirable behavior (magnetic, photoluminescent) unique to the europium while the shell makes the material insulating and highly suitable for dielectric films. Voltage tolerance and conductivity measurements were performed on the pelletized samples (Fig. 5e and 5f). Voltage tolerance/resistance was performed using a Keithley 2440 source meter. Due to the very different resistances of the two samples, the voltage ranges needed to observe the voltage

tolerance were different (EBTO-Air, was 0V to 200V, step 4V; EBTO-Argon, 0V to 10V, step 0.4V). The EBTO-Argon was significantly more conductive than EBTO-Air (resistivities of 59.54 kΩ/mm and 2133.49 GΩ/mm respectively). The terms breakdown voltage or dielectric strength are often used interchangeably to mean the point at which an insulating material breaks down or is shorted, allowing current to flow. However for nanomaterials and nanocomposites it is more practical to consider voltage tolerance, and to more closely define the voltage at which a specific level of current flow is reached which can be considered a tipping point, but may also be reversible and/or be a cause of self-healing.[70] Previous work by Yang *et al.* defines the breakdown voltage for a dielectric as the applied voltage when the leakage current exceeds 10 μA/cm^2.[70,71] The Keithley 2440 could source up to 200V and measure up to 0.1 A. Each I-V curve was fitted linearly and the voltage tolerance was extrapolated as the point where the current density crosses 10 μA/cm^2. The surface area of both materials was 1 cm^2 so the breakdown voltage could be expected to occur at 0.1 μA. From the fitting, it was determined that EBTO-Argon and EBTO-Air have voltage tolerances of 0.0234 V and 220.42 V respectively for 100 μm pellets. EBTO-Air is behaving like a conventional dielectric film with voltage tolerance of ~22 kV/cm, (2.2 Vμm^{-1}), promising for an unsintered, nanoparticulate film with no polymer filler, and notwithstanding breakdown voltage (E_B) would be considerably higher than this value. For comparison, high electric fields are considered to be > 10 Vμm^{-1}, and commercial $BaTiO_3$ based MLCC capacitors typically have dielectric layers with E_B in the range 20-30 Vμm^{-1}.[72]

Impedance spectroscopy (IS) is a powerful, non-destructive tool for the investigation of dielectric materials and can help correlate the structural and electrical characteristics of nanocrystalline materials as a function of frequency.[66,73] When contemplating a thin film composed of a nanoscale ceramic-like oxide, factors that affect permittivity values at low frequency depend greatly on processing conditions that influence grain size, grain boundaries and additional compositional features created during processing that are not necessarily intrinsic to the chemical structure of the compound. These are termed extrinsic effects. At low frequencies, typical polarization mechanisms in thin films comprised of oxide nanograins can arise from interfacial (Maxwell-Wagner-Sillars) and additional ionic space-charge effects.[74] The ε_{eff} for this region is therefore considered to be dependent on the texture of the pellet and interface between electrode and pellet; and the intrinsic behavior of the film is only one of several contributions. The result of "space-

charge" effects is that at low frequencies, ε' is dominated by the extrinsic contact capacitance, often higher than the intrinsic bulk capacitance. With increasing frequency, the intrinsic response dominates.[75] In the EBTO films, very little extrinsic contribution is observed, and they are behaving like true capacitors. The EBTO-Air reveals itself to be a very stable capacitor over the full frequency range, yielding a frequency response of the permittivity that follows an insulating dielectric, confirmed also by the voltage tolerance measurement. The response of EBTO-Argon is also stable, with slight evidence of space charge effects < 200Hz. The effective permittivity, ε_{eff} , decreases by about 23% from 132 (1 kHz) to 101 (> 1 MHz). In the 1-100 kHz regime, internal barrier layer capacitance can contribute to unusually large values of permittivity,[76,77] but by 1 MHz, it is generally the intrinsic value that is under observation. Therefore we can largely rule out contribution to ε_{eff} due to extrinsic effects and conclude that EBTO-Argon possesses an intrinsic capacitance that is 4-5x larger than the EBTO-Air counterpart. The EBTO-Argon sample also shows a lower voltage tolerance and higher conductivity by several orders of magnitude, these observations combined with the higher ε_{eff} give an indication of mobile surface electrons that are not present in EBTO-Air.

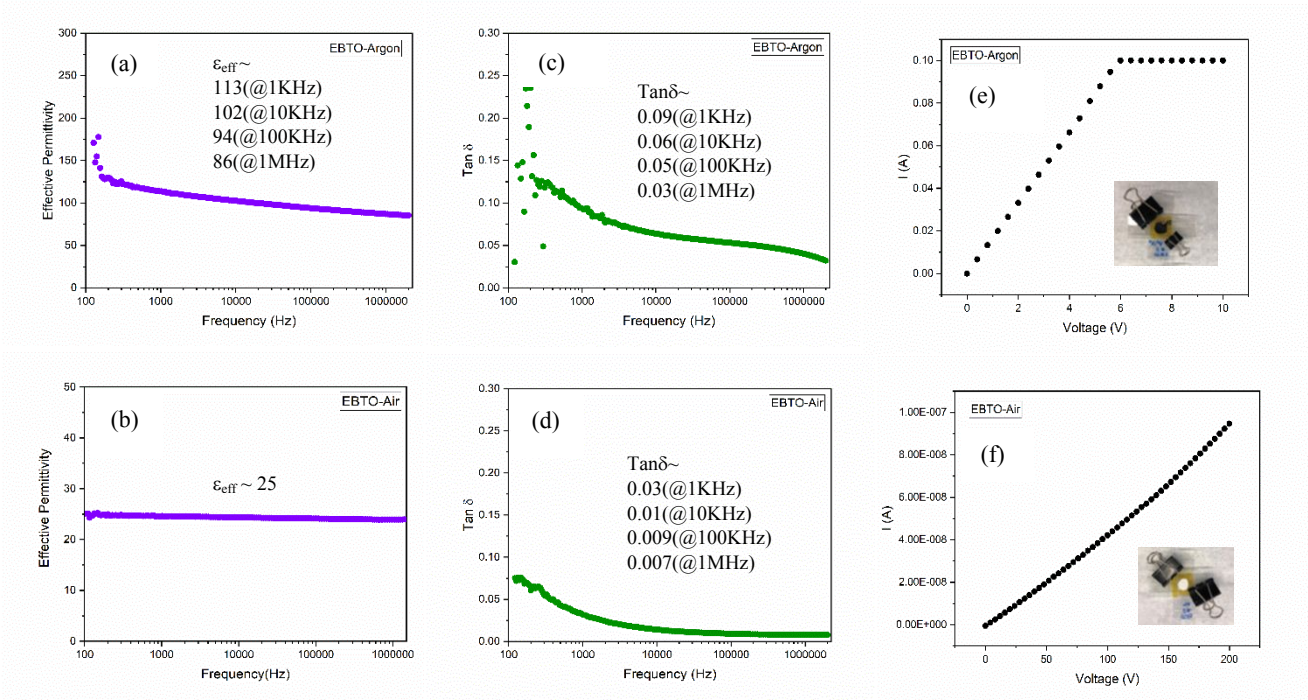

Fig. 5. a) and b) Effective permittivity, c and d) Dissipation measurements, e and f) Voltage tolerance and conductivity measurements for EBTO-Argon and EBTO-Air respectively

4. XPS Measurements

From the characterization performed, a distinctive variance in magnetic/electronic behavior was observed as a function of redox processing conditions for nanoscale $Eu_{0.5}Ba_{0.5}TiO_3$. X-ray Photoelectron Spectroscopy (XPS) analysis, including peak fitting/modeling was performed on EBTO-Air and EBTO-Argon samples in order to assess, as close as possible, the oxidation states of the elements present. All spectra presented are from a surface analysis survey and referenced to the C 1s-signal at 284.8 eV. Survey and referencing of XPS data to the C 1s-signal is, in-of-itself, an issue discussed in the literature.[78] However, given the C 1s method is standard protocol performed by the manufacturers of the Physical Electronics Versaprobe II XPS, we elected to use the referenced data as collected. Typical survey and high-resolution spectra are presented in Fig. 6 and Fig. 7, with additional data provided in the supporting information. The observed binding energies and full-widths-at-half-maximum, together with some relevant literature values (FWHM) are summarized in Table 2. XPS peaks were analyzed and fitted using MultiPak v. 9.6.0.15 software. XPS spectra for barium and oxygen in both EBTO-Argon and EBTO-Air samples confirm Ba^{2+} and O^{2-}. (See Supporting Information, Fig. S7) A broad Ba $3d_{5/2}$ peak observed in the 776-783 eV range and was fitted to two peaks at 779.4 and 778 eV for EBTO-Argon and 779.3 and 778 eV for EBTO-Air, respectively and are shown in Fig. S7 (part a and b). These values agree well with previously observed features in samples of $BaTiO_3$.[79] The deconvolution of the Ba $3d_{5/2}$ peak shows a α-bulk and β-surface species of Ba^{2+}, respectively, as Ba^{2+} is in a different chemical environment depending on if it is within the nanoparticle or on the surface. The α peak is at 779.3/779.4 eV, and the β peak is at 778 eV; these agree well with literature[68]. For O 1s there are two peaks present in both argon and air samples; one at around 528 eV and a shoulder at around 530 eV respectively, as shown in Fig. S7 (part c and d). The shoulder was attributed to the formation of surface carbonate, as perceived by the powder XRD and confirmed by FT-IR (Figure S11).

XPS Photoelectron (with Fig. no.)	EBTO-Air, observed binding energy (eV)	FWHM (eV)	EBTO-Argon, observed binding energy (eV)	Fwhm (eV)	$BaTiO_3$ and $SrTiO_3$[80,81]	TiO_2[82]	Eu:SiO_2, Eu_2O_3[83]
Ti $2p_{1/2}$ (Fig. 7)	462.9 463.9	1.45 0.86	462.9 463.9	1.34 0.97	464.6	464.0	-
Ti $2p_{3/2}$ (Fig. 7)	457.4 458	1.44 1.43	457.4 458	1.18 1	457.7-459	458.2-459.3	-
Ba $3d_{5/2}$ (Fig. S7)	778-779.4	1.56 1.58	778- 779.3	1.43 1.58	778.0-779.1	-	-

O 1s (Fig. S7)	528.8 530.2	1.33 2.18	528.9 530.3	1.3 2.43	528.8-530.3	529-532	-
Eu $3d_{3/2}$ (Fig. 6)	1155.3, 1163.4	6.05 6.36	1154.4, 1163.6	6.05 6.36	-	-	1155.9 1165.4
Eu $3d_{5/2}$ (Fig. 6)	1125, 1133.8	5.73 5.12	1124.2, 1134.1	3.5 5.03	-	-	1126.1 1135.8
Eu $4d_{3/2}$ (Fig. 6)	130 140.6	2.63 4.38	132.4 140.9	1.72 3.95	-	-	134.2, 142.9
Eu $4d_{5/2}$ (Fig. 6)	127.3, 135.1	1.94 3.36	127.6, 135.3	2.2 3.85	-	-	128.4, 137.3

Table 2. XPS peaks for $Ba_{0.5}Eu_{0.5}TiO_3$ and comparison with literature values.

Europium 3d and 4d binding energy XPS spectra for both EBTO-Air and EBTO-Argon were recorded (Fig. 6). The Eu 3d binding energies in the EBTO-Argon (Fig. 6b) are assigned to the Eu^{2+} $3d_{5/2}$(1124.3 eV), Eu^{3+} $3d_{5/2}$(1133.9 eV), Eu^{2+} $3d_{3/2}$(1154.8 eV) and Eu^{3+} $3d_{3/2}$(1163.6 eV). In the EBTO-Air sample (Fig. 6a), the Eu 3d binding energies are assigned to the Eu^{2+} $3d_{5/2}$(1124.8 eV), Eu^{3+} $3d_{5/2}$(1133.9 eV), Eu^{2+} $3d_{3/2}$(1154.9 eV) and Eu^{3+} $3d_{3/2}$(1163.2 eV). The Eu 3d spectra for both samples are almost identical and having a combination of Eu^{2+} and Eu^{3+}, however, the majority is attributed to Eu^{3+}. The Eu^{2+} $3d_{5/2}$ and Eu^{2+} $3d_{3/2}$ spin orbit components are located at 30.5 eV and 30.1 eV for EBTO-Argon and EBTO-Air respectively which are in good agreement (Δ=30 ±1 eV) with Eu in the 2+ oxidation state.[84] Similarly, the Eu^{3+} $3d_{5/2}$ and Eu^{3+} $3d_{3/2}$ spin orbit components appear at 29.7 eV and 29.3 eV for EBTO-Argon and EBTO-Air respectively which attribute to Eu in the 3+ oxidation state.[83]

The Eu 4d binding energies are also present in Fig. 6. For the EBTO-Argon sample (Fig. 6d), the peaks are assigned to the Eu^{2+} $4d_{5/2}$(126.8 eV and 128.6 eV), Eu^{2+} $4d_{3/2}$(132.8 eV), Eu^{3+} $4d_{5/2}$(135.4 eV) and Eu^{3+} $4d_{3/2}$(138.5 eV and 141.2 eV). In the case of EBTO-Air sample (Fig 6c), the Eu 4d binding energies are assigned to the Eu^{2+} $4d_{5/2}$(127.5 eV and 130.7 eV), Eu^{3+} $4d_{5/2}$(134.6 eV and 136.2 eV) and Eu^{3+} $4d_{3/2}$(140.8 eV and 141.7 eV). The Eu^{2+} $4d_{5/2}$ peak in the Argon sample and the Eu^{3+} $4d_{5/2}$ in the air sample consist of two components which most likely is attributed to the different oxidation process of europium either on the surface or the bulk. The Eu 4d graphs show a vivid difference in the air and argon samples. The EBTO-Argon has an obvious peak for Eu^{2+} $4d_{3/2}$ and $4d_{5/2}$ which is very tiny or almost absent in the case of EBTO-Air sample.

In the case of Europium XPS, we consider that it is likely more difficult to obtain fully reduced Eu^{2+}, based in part on our own experimental observations, those in the literature, and the standard reduction potential of Eu^{3+}/Eu^{2+}. Furthermore, it has been reported that

thermodynamically unstable Eu^{2+} ions are prone to be easily oxidized by H_2O and O_2, particularly under X-ray irradiation during XPS measurements[83]. In some previous cases, such as $Eu_{0.5}Ba_{0.5}TiO_3$ prepared by PLD[85], Ti^{3+} was observed by XPS, while predominantly Eu^{2+} was observed in the europium 4d XPS spectra. Very little evidence of the presence of Eu^{3+} was observed by XPS, suggesting no oxidation of Eu(II) to Eu(III) had taken place, and the conclusion was most likely $Eu_{0.5}Ba_{0.5}TiO_{3-\delta}$ with oxygen vacancies accounting for the difference and suggesting charge neutrality was maintained solely between Ti^{3+}/Ti^{4+} and oxygen, while Eu remained +2. In this case we observe the presence of Eu^{3+}, commensurate with chemical solution processing conditions and the data recorded. The observation of Eu^{3+} is unequivocal, and observed in both europium 3d and 4d XPS spectra. The ratio of Eu(II) to Eu(III) can be estimated, and there is strong indication that the amount of Eu(III) is higher in the case of the perovskite derived from air vs. Ar/H_2 ,which is to be expected. The ratio of Eu^{2+} and Eu^{3+} in each compound was calculated using the area percentage given in the Multipak software. However, since XPS is a surface analysis technique the determination is imprecise and would likely suppress true values of Eu^{2+}, since Eu^{3+} may be at more abundant at the surface. Estimations, based upon relative peak sizes and areas, lead us to conclude the following preliminary estimations of stoichiometry/oxidation state: EBTO-Air: $Eu(II)_{0.10}Eu(III)_{0.40}Ba_{0.5}Ti(IV)_{0.4}Ti(III)_{0.6}O_{3-\delta}$; EBTO-Argon: $Eu(II)_{0.15}Eu(III)_{0.35}Ba_{0.5}Ti(IV)_{0.5}Ti(III)_{0.5}O_{3-\delta}$, for which some O deficiency is incorporated, based upon expectations for such compounds, and for which $\delta < 0.1$.

The observation of a color change (from black to blue to white) when the material is opened to air, within 10 minutes at room temperature provides immediate confirmation of the materials sensitivity to environmental oxygen, and tendency of the surface Eu to be oxidized to Eu^{3+}. But interestingly, calcination to 650°C in either case allows for the crystallization of $Eu_{0.5}Ba_{0.5}TiO_3$ in the perovskite phase, unlike $EuTiO_3$.[27] In the case of EBTO-Air, the O_2 atmosphere likely generates increased Eu^{3+} at the surface but in an amorphous oxide format of approximately ~4nm thick, that ultimately converts to $Eu_2Ti_2O_7$/ Eu_2O_3 at 1000°C (see supporting information Fig. S6). The observation for EBTO-Air is that a kinetic barrier layer forms such that the majority core perovskite structure is preserved, while in the case of EBTO-Argon the perovskite structure is well preserved throughout. In both cases, however, the internal presence of Eu(II) to Eu(III) is does not cause destabilization of the potentially metastable perovskite structure, nor structural

transformation until ≥ 1000°C: the perovskite structure can be retained even with an unexpected partial quantity of Eu^{3+}.

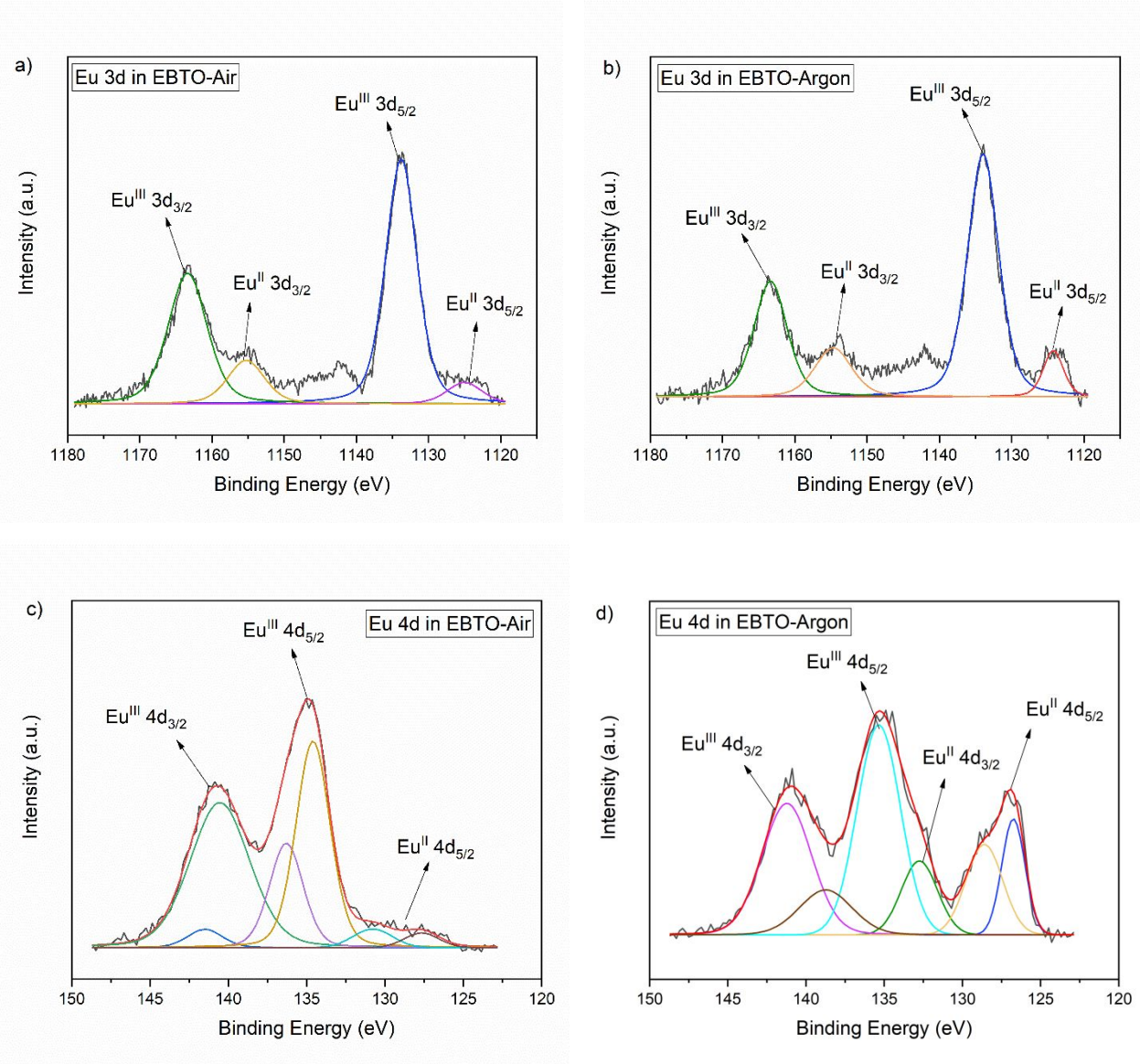

Fig. 6. XPS spectra of Europium 3d and 4d for EBTO-Argon and EBTO-Air samples

Since the Eu XPS spectra clearly shows the presence of Eu^{2+} and Eu^{3+}, we rule out the supposition that nanoscale $EuBaTiO_3$ has single oxidation states for the Transition/Lanthanide elements present. The compound is postulated to be of the form (Eu^{II}, Eu^{III})(Ba)(Ti^{III},Ti^{IV})O_3. Oxygen vacancies cannot be ruled out, although they would favor the reduced states of the metal. In the case of EBTO-Argon, such vacancies are more likely. In terms of the presence of multivalent states

of Eu and Ti, the analogy can made with pseudobinary and pseudoternary transition metal oxides, such as $La_{1-x}Sr_xTiO_3$, in which an M^{III} and M^{II} is supported by mixed valence titanium.[86] Similarly, in the $(Li,La)TiO_3$ system titanium is known to reduce its oxidation state from IV to III during electrochemical Li^+ insertion.[87] Analysis of the Ti core-level $L_{2,3}$-edge is not straightforward, as it includes both the 3s and 3d p-DOS (projected Density of States) from Ti and the initial 2p core level is split into two levels, $2p_{1/2}$ and $2p_{3/2}$, produced by spin−orbit interaction. More sophisticated methods going beyond the independent particle approximation are required for these calculations.[88] However, Ti $L_{2,3}$-edge spectra are known to be quite distinct for Ti^{4+} or Ti^{3+} in perovskite oxides.[62,86,89] The presence of Ti^{3+} results in the splitting off of a Ti t_{2g} band from the states crossing the Fermi level in LDA (Local Density Approximation).[90]

The spectra for the Ti 2p peaks is shown in Fig. 7. The Ti $2p_{1/2}$ and Ti $2p_{3/2}$ spin-orbital splitting photoelectrons for both samples are located at binding energies of 463.3 and 457.5 eV, respectively. The peak separation of 5.8 eV between the Ti $2p_{1/2}$ and Ti $2p_{3/2}$ signals is in agreement with previously reported literature values.[82] The FWHM of the Ti $2p_{1/2}$ and $2p_{3/2}$ signals are shown in Table 2. A review of published Ti 2p values for TiO_2, show that the spin-orbital splitting photoelectrons are generally located at binding energies of 458.2-459.3 eV ($2p_{1/2}$) and 464.1-465.2 eV ($2p_{3/2}$). XPS values for Ti 2p in perovskites are typically similar to those observed for TiO_2.[81,82]

Auger and Core-level photoelectron spectroscopy of Ti_2O_3, TiO_2 and $BaTiO_3$ have shown that ascribing the oxidation state to Ti tends to point to a range from +2.9 to +4, depending greatly on processing history and oxygen content.[80] Indeed, the interesting catalytic behavior of TiO_2 is partially attributed to mixed valence character.[91] Since the O 1s and Ti 2p core levels in $BaTiO_3$ and TiO_2 have generally been observed to have identical binding energies and line shapes, it is inferred that the Ti oxidation state is very similar in these two materials. We commonly tend to assume the formal oxidation state of the Titanium is 4+, represented as a maximum valence for charge neutrality in the formal stoichiometries. However, Ti-O bonding in both TiO_2 and $BaTiO_3$ has a notable degree of covalency, and while Ba^{2+} ionicity is easy to discern, it is not the case for Ti. Ti photoemission resonances, and corresponding electronic structure calculations and Raman data have previously confirmed charge density distortion around the Ti-cation in perovskites.[80] Electronic structure calculations in TiO_2 support O 2p 3d hybridization with Ti 3d contributing significantly to the valence band, while the conduction band is also composed of both Ti 3d and O 2p states.[91] Cluster model predictions[62] for the net d-electron occupancy n_d for the formally d^0

compounds $SrTiO_3$, TiO_2, yield n_d = 1.0 –1.5, indicating a large covalency in the Ti with considerable charge transferred from the oxygen sites to the metal sites. The strong covalency is mainly due to the large value of $pd\sigma$. This is in agreement with band-structure calculations predicting a significant Ti-O hybridization for the Ti oxides. Recent calculations indicate that the ferroelectricity in $BaTiO_3$ is driven by charge distortions around the Ti cation sites, which would also support considerable charge transfer from the O sites.[22] Similar hybridization calculations (including *ab initio* Hartree-Fock) and comparison with experimental observations for X-ray photoemission spectra have been performed for the series TiO, TiO_2, Ti_2O_3, for which n_d is found to range from 2.6 to 1.7/1.6, as ionicity decreases along the series.[62] In TiO_2 with oxygen deficiencies or Ti_2O_3, an abundance of core holes, poorly screened final states (including surface states) leads to the observation of lower photoelectron binding energies than the Ti 2p levels in TiO_2/$BaTiO_3$, by ~1eV.[80] This positive, initial-state chemical shift can be identified as a valence of +3. We subsequently hypothesize, and model successfully a fitting of titanium that corresponds to a mixture of valence states of between +3 to +4.

Ti 2p XPS spectra and fitting is presented in Fig. 7. This fit is an assumed combination of Ti^{3+} and Ti^{4+} in both EBTO air and argon samples, with different ratios of the Ti^{4+}/Ti^{3+} (increased in EBTO-Argon). The XPS spectra shows the Ti^{3+} $2p_{3/2}$ peak at around 457 eV and the other peak for the doublet Ti^{3+} $2p_{1/2}$ at around 462 eV. For the Ti^{4+}, the Ti^{4+} $2p_{3/2}$ peak is present at around 458 eV and the Ti^{4+} $2p_{1/2}$ peak at around 463 eV. The Ti peak areas were calculated by Multipak and compared with the Eu^{3+}/Eu^{2+} ratio. The relative ratios of Ti^{4+}/Ti^{3+} are estimated to be : 50%-50% for EBTO-Argon and 40%-60% for the EBTO-Air sample, leading to an average of oxidation state of +3.4-3.5, and to proposed n_d values of 0.5-0.6, well within range of other compounds with known Ti-O covalency.

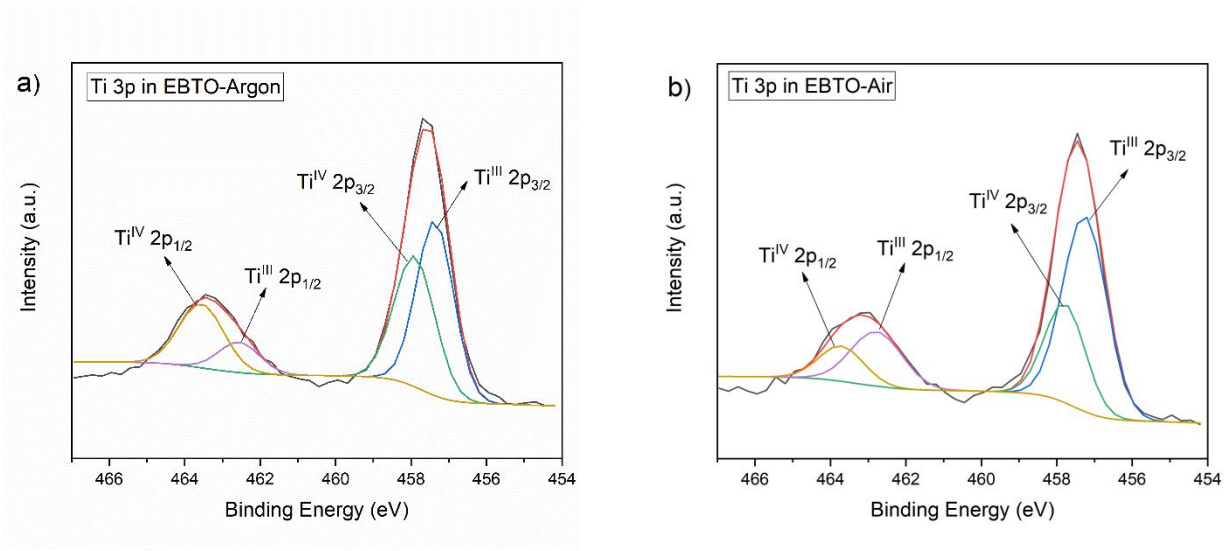

Fig. 7. XPS spectra of Titanium 2p for EBTO-Argon(a) and EBTO-Air(b) samples

Optical Characterization

Complex transition metal perovskite oxides represent a wide range of electronic properties, including the possibility of a tunable band gap[92,93,94]. Changes in the local environments and control over the Eu valence states (Eu^{3+}/Eu^{2+}) in phosphor materials to tune their activation have been extensively investigated with the aim of improving the materials' photoluminescence (PL) properties.[95] Furthermore, the PL of lanthanide metals in ferroelectric perovskites has indicated sensitivity to the polarization environment.[96] For the evaluation of the optical features, diffuse reflectance (DR) spectra of EBTO Air and Argon samples was obtained and had broad absorption bands from UV to NIR (200-800 nm). The measurements, collected using a CARY 500 spectrophotometer equipped with a diffuse reflectance accessory (integrating sphere), shown in Fig. 8a. The light absorption of EBTO-Air occurs below 430 nm, while, in contrast, EBTO-Argon (black) shows an elevated light absorption across the entire range (Fig. 8b). The absorbance/reflectance data confirm what is observable to the eye, that the EBTO-Argon sample is strongly absorbing across the visible range while the EBTO-Air sample absorbs significantly less light across the visible (400-800 nm) with much higher light scattering, giving rise to much higher reflectance (65% vs < 10%). To obtain a quantitative evaluation of the visible absorption profile, the indirect optical band gaps (E_g) values were estimated by applying the Kubelka-Munk function[97] by extrapolating the linear portion of $(F(R)*h\upsilon)^2$ versus $h\upsilon$ plots to intercept the photon

energy[98] (Tauc plots in Fig. 8c) and were calculated to be of 3.31 eV and 3.42 eV for EBTO-Ar/H_2 and EBTO-air respectively. A higher band gap for EBTO-Air is commensurate with the observations of lower absorbance and more insulating character. These values, suggestive of potential photoactivity, are similar to reported values for Barium titanate nanoparticles,[92] while the differences might be considered interesting for possible variations in catalytic activity. In the case of EBTO-Argon, a stronger light absorbance was revealed at around 390 nm, suggesting that the differences in the surface chemistry affect the optical properties, supported by the slightly lower in value E_g of 3.31 eV.

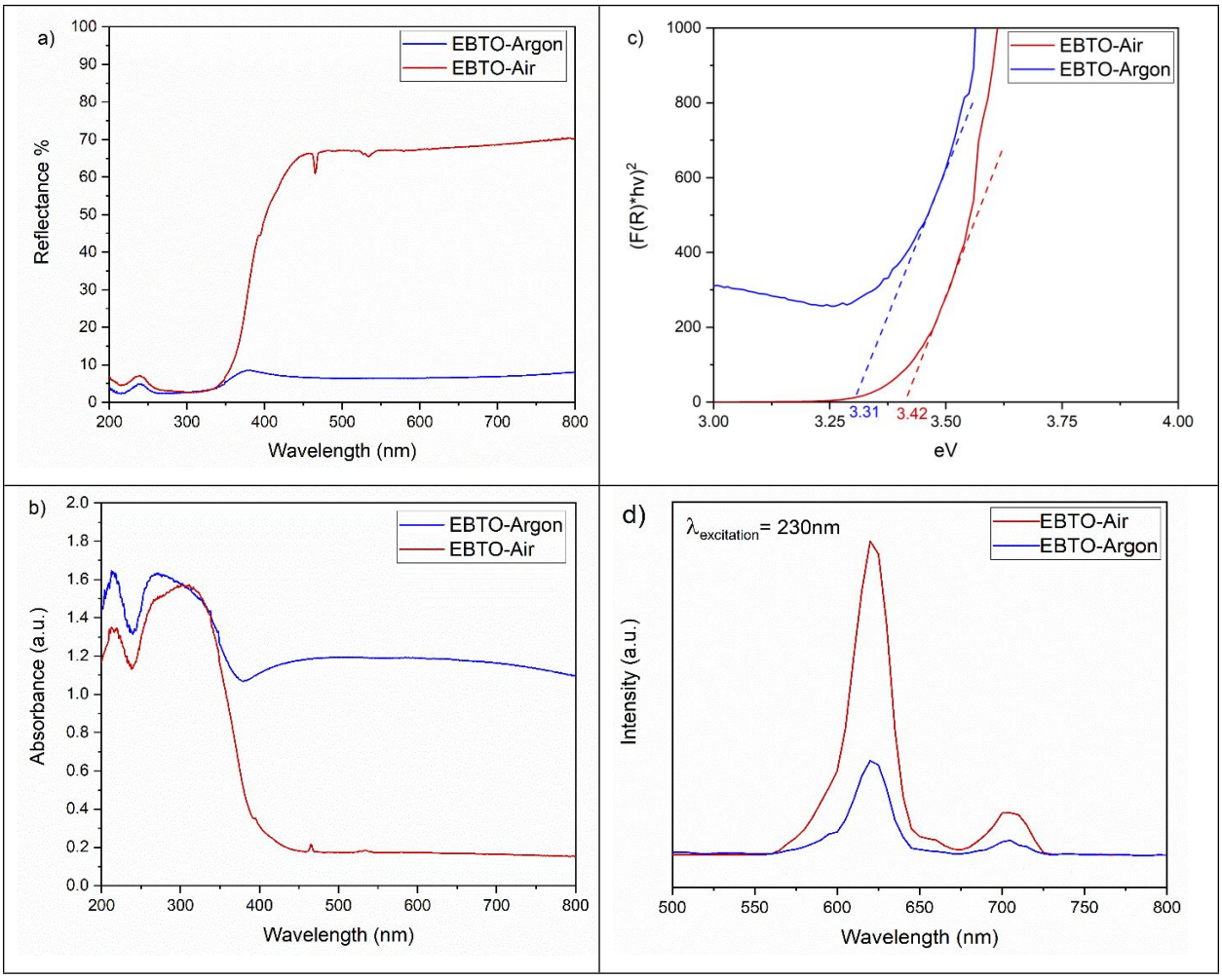

Fig. 8. a) Reflectance, b) Absorbance and c) Tauc plot d) PL spectra for EBTO-Argon(blue) and EBTO-Air(red)

The room temperature photoluminescence (PL) emission spectra of the nanocrystalline EBTO (Air and Argon) samples excited with 230 nm wavelength are shown in Fig. 8d. The spectra was collected using Spectramax id5 instrument (Molecular Devices). 1 mg of the EBTO nanoparticles

were suspended into 1 ml DI water through cup horn sonication. Then a 1 mg/ml of nanoparticle solution was transferred into a quartz cuvette. Photoluminescence emission peaks observed in the 500-800 nm region are assigned to their transitions in Fig. 9 a. These transitions are emissions from the typical $^5D_0$ excited state to the ^7F_J (J=0-4) ground state levels which are the response from Eu^{3+} in both samples.[99] The emission peaks are located at 602 nm, 622 nm, 657 nm and 703 nm which are related to $^5D_0 \rightarrow {}^7F_1$, $^5D_0 \rightarrow {}^7F_2$, $^5D_0 \rightarrow {}^7F_3$ and $^5D_0 \rightarrow {}^7F_4$ transitions respectively. Our data is in good agreement with previously reported values (with a slight variation of excitation wavelength of around 20 nm).[99] Also, it has reported that by increasing the excitation wavelength to 395 nm, another peak is found for the $^5D_0 \rightarrow {}^7F_0$ transition at around 610 nm.[100] The most intense transition in the luminescence spectrum is the $^5D_0 \rightarrow {}^7F_2$ at around 622 nm leading to a strong red fluorescense.[101,102,50] This intense red luminescence of Eu^{3+} transition is useful for photoelectric devices and optical communications.[98]

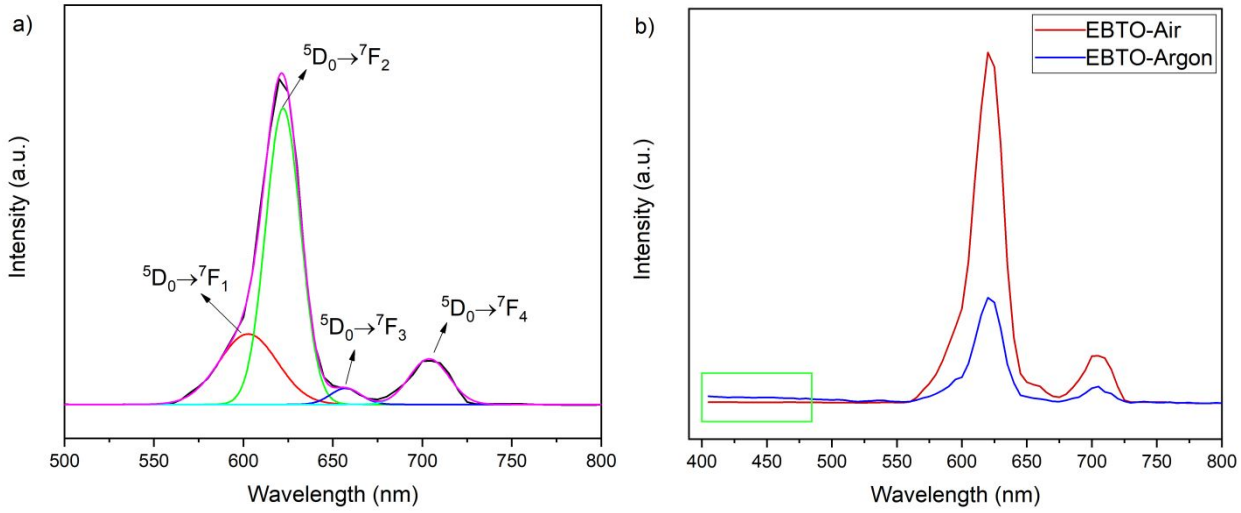

Fig. 9. (a) Fitted curve of Photoluminescence (PL) spectra for the EBTO; (b) Comparison of PL spectra of EBTO-Air and EBTO-Argon.

Fig. 9 presents the emission transitions in detail in Fig. 9a and the comparison of EBTO-Air and argon samples in Fig. 9b. Eu^{3+} emission is confirmed for both, and the amount of Eu^{3+} is clearly higher in EBTO-Air, in agreement with XPS. There is a slight elevation at lower wavelengths for EBTO-Argon the (Fig. 9b, green rectangle) which could be attributed to Eu^{2+}. Eu^{2+} has broad emission bands in the visible and NIR regions originating from the 4f-5d transitions at around

420 nm and 445 nm, corresponding to $4f^6 5d^1 \rightarrow 4f^7$(out of the range for this current measurement).[100] The relative intensities of Eu^{2+}/Eu^{3+} vary with excitation wavelength: Baran. A. *et al*[103] showed that decreasing excitation energy can increase Eu^{2+} emission, confirmed by Xie, H. *et al.*[104] In general, luminescence of Eu^{3+} gives a red component to the blue/green luminescence of Eu^{2+}. As a result, when Eu^{2+} and Eu^{3+} coexist in a compound, these materials can be promising candidates for white phosphors for LEDs.[95,105] The unique optical features of Europium also make it promising as a label in nanocarriers for biomedical sensing and imaging field applications, especially when utilized in a nanoparticle delivery platform.[106–108] The $^5D_0 \rightarrow {}^7F_2$ transition has a narrow emission at 620 nm (Fig. 8d) which can penetrate tissue or hemoglobin.[109,110] A second attractive feature is that the span of the absorption/excitation wavelength is relatively large when compared to other lanthanide elements, making Eu an excellent scintillator for radioluminescence.[111] Since perovskite oxide nanoparticles are being developed for their potential as CT contrast agent nanocarriers,[112] the incorporation of Eu might improve potential for imaging. The EBTO-Air sample has a stronger red-light emission compared to EBTO-Argon. Overall, both EBTO-Argon and EBTO-Air nanoparticle suspensions present promising luminescent opportunities properties in the context of nanocomposites for phosphors and nanocarriers for biomedical applications.

Conclusion

In conclusion, nanocrystalline $Eu_{0.5}Ba_{0.5}TiO_3$ was prepared, based on a ($Eu^{II}_{x/2}Eu^{III}_{1-x/2}Ba_{1/2}Ti^{III}_{y/2}Ti^{IV}_{1-y/2}O_{3-\delta}$) system. Starting from metallic $Ba_{(s)}$ and $Eu_{(s)}$, molecular Ba/Eu alkoxide precursors were synthesized and reacted with $Ti(OCH(CH_3)_2)_4$ in the absence of O_2/H_2O. Creation of a gel monolith is initiated with the addition of a stoichiometric quantity of H_2O. The reactivity of $Ti(OCH(CH_3)_2)_4$ rapidly drives the formation of an amorphous Eu-Ba-Ti-O-OR network which serves as the template for TiO_6 octahedra oxolation and ultimate perovskite (Eu,Ba)TiO_3 formation at 650°C, lower than anticipated solid state processing temperatures and with retention of a nanoparticulate morphology. The relatively low crystallization temperature enables the isolation of the nanoscale perovskite nanoparticles suitable for suspension in alcohol solvents. Samples were treated in two different thermal environments depending on the presence or absence of oxygen (EBTO-Air and EBTO-Argon respectively). X-ray powder diffraction confirms the perovskite phase, stable up to 1000 °C,

while TEM demonstrated the ability to prepare isolated nanoparticles in the 20-40nm size range. EDS elemental mapping confirmed the presence of all elements and a uniform composition of Eu, Ba, Ti and O. XPS analysis confirms the presence of Eu^{3+}/Eu^{2+} in both samples. As a counterpoint, we conjecture and model a complimentary charge balanced configuration of Ti^{3+}/Ti^{4+}. The amount of Eu^{3+}/Ti^{3+} was higher in EBTO-Air sample, compared to the EBTO-Argon, to account for a charge compensated perovskite. $Eu_{0.5}Ba_{0.5}TiO_3$ prepared under Air/O_2 atmospheres produced a spherical core-shell nanostructure, with perovskite $Eu_{0.5}Ba_{0.5}TiO_3$ nanocrystal core (~30 nm) - insulating oxide shell-layer (~2-4 nm), presumed a pre-pyrochlore layer abundant with Eu^{3+}. Fluorescence spectroscopy shows a high intensity $^5D_0 \rightarrow {}^7F_2$ transition at 622 nm and strong red fluorescence. The core/shell structure demonstrated excellent capacitive properties: assembly into dielectric thin films gave low conductivity (2133 GΩ/mm) and an extremely stable, low loss permittivity of ε_{eff} ~25 over a wide frequency range ($\tan\delta < 0.01$, 100 kHz - 2 MHz). $Eu_{0.5}Ba_{0.5}TiO_3$ prepared under H_2/Argon produced more irregular shaped nanocrystals (~20 nm), with a thin film permittivity around 4 times greater but marginally higher loss and much lower dielectric strength (ε_{eff} 101, $\tan\delta$ <0.05, 10 KHz-2 MHz, σ ~59.54 kΩ/mm). Field-cooled Magnetization values of 0.025 emu/g (EBTO-Air) and 0.84 emu/g for EBTO-Argon were observed. Magnetic characterization by MPMS (both hysteresis loops and zero field and field cooling measurements) showed higher magnetization for the EBTO-Argon samples which has higher amount of Eu^{2+} than EBTO-Air sample which mainly consists of Eu^{3+} and related to the higher number of lone pairs in the $4f^7$ electronic configuration in the Eu^{2+}. Both samples showed a decrease in magnetization by increasing the temperature. Photoluminescence emission from the typical $^5D_0$ excited state to the ^7F_J (J=0-4) ground state levels confirms the presence of Eu^{3+} in both samples, but much higher in EBTO-Air. The emission peaks are observed for the $^5D_0 \rightarrow {}^7F_1$, $^5D_0 \rightarrow {}^7F_2$, $^5D_0 \rightarrow {}^7F_3$ and $^5D_0 \rightarrow {}^7F_4$ transitions, in good agreement with previously reported values.

Acknowledgements

This work was supported by the National Science Foundation, under NSF DMR award #1461499, and with support from NSF CREST #1547830. All magnetic characterization was conducted at the Center for Nanophase Materials Sciences, Oak Ridge National Laboratory, which is a DOE

Office of Science User Facility (supported under Project Number CNMS2017-211). S.O. is grateful to the PSC-CUNY Research Awards Program for additional support. S.O., N.F. and Q.Z. are grateful to Dr. Jan Grimm (Memorial Sloan Kettering Cancer Center) for providing access to their spectrophotometer, and for providing useful discussion regarding the potential biomedical utility of Eu containing nanoparticles. C.K.M is grateful for support from the National Science Foundation Graduate Research Fellowship Program: DGE - 1644869. S.O. thanks Terry Williams for useful discussions over the years, regarding matter-antimatter asymmetry.

ORCID ID NUMBERS

Stephen O'Brien: https://orcid.org/0000-0001-7531-8900

Nasim Farahmand: https://orcid.org/0000-0001-7543-6886

Ioannis (John) Kymissis: https://orcid.org/0000-0001-7417-1759

Christine K. McGinn: https://orcid.org/0000-0002-5294-6346

Zheng Gai: https://orcid.org/0000-0002-6099-4559

Qize Zhang: https://orcid.org/0000-0002-7345-7744

References

(1) Scott, J. F. Searching for New Ferroelectrics and Multiferroics: A User's Point of View. *npj Comput. Mater.* **2015**, *1* (July), 1–9. https://doi.org/10.1038/npjcompumats.2015.6.

(2) Bussmann-Holder, A.; Köhler, J. Revisiting the Fascinating Properties of EuTiO3 and Its Mixed Crystals with $SrTiO_3$: Possible Candidates for Novel Functionalities. *J. Phys. Chem. Solids* **2015**, *84* (1), 2–12. https://doi.org/10.1016/j.jpcs.2014.12.019.

(3) Sushkov, A. O.; Eckel, S.; Lamoreaux, S. K. Prospects for an Electron Electric-Dipole-Moment Search with Ferroelectric (Eu,Ba)TiO_3 Ceramics. *Phys. Rev. A - At. Mol. Opt. Phys.* **2010**, *81* (2). https://doi.org/10.1103/PhysRevA.81.022104.

(4) Spaldin, N. A. Multiferroics: Past, Present, and Future. *MRS Bull.* **2017**, *42* (5), 385–389. https://doi.org/10.1557/mrs.2017.86.

(5) Eckel, S.; Sushkov, A. O.; Lamoreaux, S. K. Limit on the Electron Electric Dipole Moment Using Paramagnetic Ferroelectric $Eu_{0.5}Ba_{0.5}TiO_3$. *Phys. Rev. Lett.* **2012**, *109* (19),

1–5. https://doi.org/10.1103/PhysRevLett.109.193003.

(6) Yu, P.; Chu, Y. H.; Ramesh, R. Emergent Phenomena at Multiferroic Heterointerfaces. *Philos. Trans. A. Math. Phys. Eng. Sci.* **2012**, *370* (1977), 4856–4871. https://doi.org/10.1098/rsta.2012.0199.

(7) Goian, V.; Kamba, S.; Pacherová, O.; Drahokoupil, J.; Palatinus, L.; Duek, M.; Rohlíček, J.; Savinov, M.; Laufek, F.; Schranz, W.; Fuith, A.; Kachlík, M.; MacA, K.; Shkabko, A.; Sagarna, L.; Weidenkaff, A.; Belik, A. A. Antiferrodistortive Phase Transition in $EuTiO_3$. *Phys. Rev. B - Condens. Matter Mater. Phys.* **2012**, *86* (5), 1–9. https://doi.org/10.1103/PhysRevB.86.054112.

(8) Kim, J. W.; Thompson, P.; Brown, S.; Normile, P. S.; Schlueter, J. A.; Shkabko, A.; Weidenkaff, A.; Ryan, P. J. Emergent Superstructural Dynamic Order Due to Competing Antiferroelectric and Antiferrodistortive Instabilities in Bulk $EuTiO_3$. *Phys. Rev. Lett.* **2013**, *110* (2), 1–5. https://doi.org/10.1103/PhysRevLett.110.027201.

(9) Katsufuji, T.; Takagi, H. Coupling between Magnetism and Dielectric Properties in Quantum Paraelectric $EuTiO_3$. *Phys. Rev. B* **2001**, *64* (5), 054415. https://doi.org/10.1103/PhysRevB.64.054415.

(10) Rushchanskii, K. Z.; Kamba, S.; Goian, V.; Vanek, P.; Savinov, M.; Prokleska, J.; Nuzhnyy, D.; Knízek, K.; Laufek, F.; Eckel, S.; Lamoreaux, S. K.; Sushkov, A. O.; Lezaić, M.; Spaldin, N. A. A Multiferroic Material to Search for the Permanent Electric Dipole Moment of the Electron. *Nat. Mater.* **2010**, *9* (8), 649–654. https://doi.org/10.1038/nmat2799.

(11) CERN. The Matter-Antimatter Asymmetry Problem, Https://Home.Cern/Science/Physics/Matter-Antimatter-Asymmetry-Problem.

(12) Eerenstein, W.; Mathur, N. D.; Scott, J. F. Multiferroic and Magnetoelectric Materials. *Nature* **2006**, *442* (7104), 759–765. https://doi.org/10.1038/nature05023.

(13) Srinivasan, G. Magnetoelectric Composites. *Annu. Rev. Mater. Res.* **2010**, *40* (1), 153–178. https://doi.org/10.1146/annurev-matsci-070909-104459.

(14) Khomskii, D. I. Multiferroics: Different Ways to Combine Magnetism and Ferroelectricity. *J. Magn. Magn. Mater.* **2006**, *306* (1), 1–8. https://doi.org/10.1016/j.jmmm.2006.01.238.

(15) Hill, N. A. Why Are There so Few Magnetic Ferroelectrics? *J. Phys. Chem. B* **2000**, *104*

(29), 6694–6709. https://doi.org/10.1021/jp000114x.

(16) Weston, L.; Cui, X. Y.; Ringer, S. P.; Stampfl, C. Multiferroic Crossover in Perovskite Oxides. *Phys. Rev. B* **2016**, *93* (16), 1–11. https://doi.org/10.1103/PhysRevB.93.165210.

(17) Rao, C. N. R.; Sundaresan, A.; Saha, R. Multiferroic and Magnetoelectric Oxides: The Emerging Scenario. *J. Phys. Chem. Lett.* **2012**, *3* (16), 2237–2246. https://doi.org/10.1021/jz300688b.

(18) Janes, D. L.; Bodnar, R. E.; Taylor, A. L. Europium Barium Titanate - A Magnetic Ferroelectric Compound. *J. Appl. Phys.* **1978**, *49* (3), 1452–1454. https://doi.org/10.1063/1.324974.

(19) Polking, M. J.; Han, M. G.; Yourdkhani, A.; Petkov, V.; Kisielowski, C. F.; Volkov, V. V.; Zhu, Y.; Caruntu, G.; Paul Alivisatos, A.; Ramesh, R. Ferroelectric Order in Individual Nanometre-Scale Crystals. *Nat. Mater.* **2012**, *11* (8), 700–709. https://doi.org/10.1038/nmat3371.

(20) Shi, C.; Billinge, S. J. L.; Puma, E.; Bang, S. H.; Bean, N. J. H.; De Sugny, J. C.; Gambee, R. G.; Haskell, R. C.; Hightower, A.; Monson, T. C. Barium Titanate Nanoparticles: Short-Range Lattice Distortions with Long-Range Cubic Order. *Phys. Rev. B* **2018**, *98* (8), 1–13. https://doi.org/10.1103/PhysRevB.98.085421.

(21) Nuraje, N.; Su, K. Perovskite Ferroelectric Nanomaterials. *Nanoscale* **2013**, *5* (19), 8752–8780. https://doi.org/10.1039/c3nr02543h.

(22) Bersuker, I. B. Pseudo-Jahn-Teller Effect - A Two-State Paradigm in Formation, Deformation, and Transformation of Molecular Systems and Solids. *Chem. Rev.* **2013**, *113* (3), 1351–1390. https://doi.org/10.1021/cr300279n.

(23) Fernández-Pacheco, A.; Streubel, R.; Fruchart, O.; Hertel, R.; Fischer, P.; Cowburn, R. P. Three-Dimensional Nanomagnetism. *Nat. Commun.* **2017**, *8*, 15756. https://doi.org/10.1038/ncomms15756.

(24) Jiang, B.; Iocozzia, J.; Zhao, L.; Zhang, H.; Harn, Y. W.; Chen, Y.; Lin, Z. Barium Titanate at the Nanoscale: Controlled Synthesis and Dielectric and Ferroelectric Properties. *Chem. Soc. Rev.* **2019**, *48* (4), 1194–1228. https://doi.org/10.1039/c8cs00583d.

(25) Parija, A.; Waetzig, G. R.; Andrews, J. L.; Banerjee, S. Traversing Energy Landscapes Away from Equilibrium: Strategies for Accessing and Utilizing Metastable Phase Space. *J. Phys. Chem. C* **2018**, *122* (45), 25709–25728. https://doi.org/10.1021/acs.jpcc.8b04622.

(26) Wall, M. A.; Harmsen, S.; Pal, S.; Zhang, L.; Arianna, G.; Lombardi, J. R.; Drain, C. M.; Kircher, M. F. Surfactant-Free Shape Control of Gold Nanoparticles Enabled by Unified Theoretical Framework of Nanocrystal Synthesis. *Adv. Mater.* **2017**, *29* (21). https://doi.org/10.1002/adma.201605622.

(27) Henderson, N. L.; Baek, J.; Halasyamani, P. S.; Schaak, R. E. Ambient-Pressure Synthesis of SHG-Active $Eu_2Ti_2O_7$ with a [110] Layered Perovskite Structure: Suppressing Pyrochlore Formation by Oxidation of Perovskite-Type EuTiO3. *Chem. Mater.* **2007**, *19* (8), 17–19.

(28) Rabuffetti, F. A.; Culver, S. P.; Lee, J. S.; Brutchey, R. L. Local Structural Investigation of Eu3+-Doped $BaTiO_3$ Nanocrystals. *Nanoscale* **2014**, *6* (5), 2909–2914. https://doi.org/10.1039/c3nr06610j.

(29) Li, J.; Kuwabara, M. Preparation and Luminescent Properties of Eu-Doped $BaTiO_3$ Thin Films by Sol-Gel Process. *Sci. Technol. Adv. Mater.* **2003**, *4*, 143–148. https://doi.org/10.1016/S1468-6996(03)00027-5.

(30) Li, W.; He, Q.; Wang, L.; Zeng, H.; Bowlan, J.; Ling, L.; Yarotski, D. A.; Zhang, W.; Zhao, R.; Dai, J.; Gu, J.; Shen, S.; Guo, H.; Pi, L.; Wang, H.; Wang, Y.; Velasco-Davalos, I. A.; Wu, Y.; Hu, Z.; Chen, B.; Li, R. W.; Sun, Y.; Jin, K.; Zhang, Y.; Chen, H. T.; Ju, S.; Ruediger, A.; Shi, D.; Borisevich, A. Y.; Yang, H. Manipulating Multiple Order Parameters via Oxygen Vacancies: The Case of $Eu_{0.5}Ba_{0.5}TiO_{3-\delta}$. *Phys. Rev. B* **2017**, *96* (11), 1–7. https://doi.org/10.1103/PhysRevB.96.115105.

(31) Guichard, F.; Church, T. M.; Treuil, M.; Jaffrezic, H. Rare Earths in Barites: Distribution and Effects on Aqueous Partitioning. *Geochim. Cosmochim. Acta* **1979**, *43* (7), 983–997. https://doi.org/10.1016/0016-7037(79)90088-7.

(32) Pan, Y.; Xie, X.; Huang, Q.; Gao, C.; Wang, Y.; Wang, L.; Yang, B.; Su, H.; Huang, L.; Huang, W. Inherently Eu^{2+}/Eu^{3+} Codoped Sc_2O_3 Nanoparticles as High-Performance Nanothermometers. *Adv. Mater.* **2018**, *30* (14), 3–8. https://doi.org/10.1002/adma.201705256.

(33) Wertheim, G. K.; Sampathkumaran, E. V.; Laubschat, C.; Kaindl, G. Final-State Effects in the X-Ray Photoemission Spectrum of $EuPd_2P_2$. *Phys. Rev. B* **1985**, *31* (10), 6836–6839. https://doi.org/10.1103/PhysRevB.31.6836.

(34) Hreniak, D. Structure, Spectroscopy and Dielectric Properties of $BaTiO_3:Eu^{3+}$

Nanocrystallites Prepared by the Sol-Gel Method. *Mater. Sci. Pol.* **2002**, *20* (1), 43–50.

(35) Jha, P. A.; Jha, A. K. Influence of Processing Conditions on the Grain Growth and Electrical Properties of Barium Zirconate Titanate Ferroelectric Ceramics. *J. Alloys Compd.* **2012**, *513*, 580–585. https://doi.org/10.1016/j.jallcom.2011.11.012.

(36) Liu, S. Y.; Huang, L. M.; Li, W. L.; Liu, X. H.; Jing, S.; Li, J.; O'Brien, S. Green and Scalable Production of Colloidal Perovskite Nanocrystals and Transparent Sols by a Controlled Self-Collection Process. *Nanoscale* **2015**, *7* (27), 11766–11776. https://doi.org/10.1039/c5nr02351c.

(37) Lombardi, J.; Yang, L.; Pearsall, F. A.; Farahmand, N.; Gai, Z.; Billinge, S. J. L.; O'Brien, S. Stoichiometric Control over Ferroic Behavior in $Ba(Ti_{1-x}Fe_x)O_3$ Nanocrystals. *Chem. Mater.* **2019**, *31* (4), 1318–1335. https://doi.org/10.1021/acs.chemmater.8b04447.

(38) Hao, Y. N.; Bi, K.; O'Brien, S.; Wang, X. X.; Lombardi, J.; Pearsall, F.; Li, W. L.; Lei, M.; Wu, Y.; Li, L. T.; Wud, Y.; Lic, L. T. Interface Structure, Precursor Rheology and Dielectric Properties of $BaTiO_3$/PVDF-Hfp Nanocomposite Films Prepared from Colloidal Perovskite Nanoparticles. *RSC Adv.* **2017**, *7* (52), 32886–32892. https://doi.org/10.1039/c7ra03250a.

(39) Lombardi, J.; Pearsall, F.; Li, W.; O'Brien, S. Synthesis and Dielectric Properties of Nanocrystalline Oxide Perovskites, [KNbO3]1-x[BaNi0.5Nb0.5O3- δ]x, Derived from Potassium Niobate KNbO3 by Gel Collection. *J. Mater. Chem. C* **2016**, *4* (34), 7989–7998. https://doi.org/10.1039/c6tc02327d.

(40) Liu, S.; Akbashev, A. R.; Yang, X.; Liu, X.; Li, W.; Zhao, L.; Li, X.; Couzis, A.; Han, M.-G.; Zhu, Y.; Krusin-Elbaum, L.; Li, J.; Huang, L.; Billinge, S. J. L.; Spanier, J. E.; O'Brien, S. Hollandites as a New Class of Multiferroics. *Sci. Rep.* **2014**, *4*, 6203. https://doi.org/10.1038/srep06203.

(41) Das, R. N.; Markovich, V. R. Nanomaterials for Electronic Packaging : Toward Extreme Miniaturization. *IEEE Nanotechnol. Mag.* **2010**, *Dec*, 18–24.

(42) Kim, J. Y.; Voznyy, O.; Zhitomirsky, D.; Sargent, E. H. 25th Anniversary Article: Colloidal Quantum Dot Materials and Devices: A Quarter-Century of Advances. *Adv. Mater.* **2013**, *25* (36), 4986–5010. https://doi.org/10.1002/adma.201301947.

(43) Fortunato, E.; Barquinha, P.; Martins, R. Oxide Semiconductor Thin-Film Transistors: A Review of Recent Advances. *Adv. Mater.* **2012**, *24* (22), 2945–2986.

https://doi.org/10.1002/adma.201103228.

(44) Kamba, S.; Nuzhnyy, D.; Vank, P.; Savinov, M.; Kníek, K.; Shen, Z.; Šantaý, E.; MacA, K.; Sadowski, M.; Petzelt, J. Magnetodielectric Effect and Optic Soft Mode Behaviour in Quantum Paraelectric $EuTiO_3$ Ceramics. *EPL (Europhysics Lett.* **2007**, *80* (2), 27002. https://doi.org/10.1209/0295-5075/80/27002.

(45) Fennie, C. J.; Rabe, K. M. Magnetic and Electric Phase Control in Epitaxial $EuTiO_3$ from First Principles. *Phys. Rev. Lett.* **2006**, *97* (26), 1–4. https://doi.org/10.1103/PhysRevLett.97.267602.

(46) Goian, V.; Kamba, S.; Nuzhnyy, D.; Vaněk, P.; Kempa, M.; Bovtun, V.; Knížek, K.; Prokleška, J.; Borodavka, F.; Ledinský, M.; Gregora, I. Dielectric, Magnetic and Structural Properties of Novel Multiferroic $Eu_{0.5}Ba_{0.5}TiO_3$ Ceramics. *J. Phys. Condens. Matter* **2011**, *23* (2). https://doi.org/10.1088/0953-8984/23/2/025904.

(47) Sitko, D.; Garbarz-Glos, B.; Piekarczyk, W.; Śmiga, W.; Antonova, M. The Effects of the Additive of Eu Ions on Elastic and Electric Properties of $BaTiO_3$ Ceramics. *Integr. Ferroelectr.* **2016**, *173* (1), 31–37. https://doi.org/10.1080/10584587.2016.1183413.

(48) Lu, D. Y.; Sugano, M.; Su, W. H.; Koda, T. X-Ray Powder Diffraction Structural Characterization of $Ba_{1-x}Eu_xTiO_3$ Ternary Oxides. *Cryst. Res. Technol.* **2005**, *40* (7), 703–708. https://doi.org/10.1002/crat.200410412.

(49) Piezoelectric, L.; Fabricated, C.; Takahashi, H.; Numamoto, Y.; Takeuchi, H.; Jyomura, S.; Jian-xiu, X.; Liang, Z.; Batio, D. R.; Resonance, E. S. Electron Spin Resonance Investigations and Compensation Mechanism of Europium-Doped Barium Titanate Ceramics. **2006**. https://doi.org/10.1143/JJAP.45.8782.

(50) Hernández, M. G.; Chadeyron, G.; Boyer, D.; García-Murillo, A.; Carrillo-Romo, F.; Mahiou, R.; García-Hernández, M.; Chadeyron, G.; Boyer, D.; García-Murillo, A.; Carrillo-Romo, F.; Mahiou, R. Hydrothermal Synthesis and Characterization of Europium-Doped Barium Titanate Nanocrystallites. *Nano-Micro Lett.* **2013**, *5* (1), 57–65. https://doi.org/10.3786/nml.v5i1.p57-65.

(51) Rabuffetti, F. a; Brutchey, R. L. Complex Perovskite Oxide Nanocrystals: Low-Temperature Synthesis and Crystal Structure. *Dalton Trans.* **2014**, *43* (39), 14499–14513. https://doi.org/10.1039/c4dt01376j.

(52) O'Brien, S.; Murray, C. B.; Brus, L. E. Synthesis of Monodisperse Nanoparticles of

Barium Titanate: Toward a Generalized Strategy of Oxide Nanoparticle Synthesis. *J. Am. Chem. Soc.* **2001**, *123* (9), 12085–12086. https://doi.org/10.1021/ja011414a.

(53) Huang, L.; Chen, Z.; Wilson, J. D.; Banerjee, S.; Robinson, R. D.; Herman, I. P.; Laibowitz, R.; O'Brien, S. Barium Titanate Nanocrystals and Nanocrystal Thin Films: Synthesis, Ferroelectricity, and Dielectric Properties. *J. Appl. Phys.* **2006**, *100* (3), 1–10. https://doi.org/10.1063/1.2218765.

(54) Carretas, J. M.; Branco, J.; Marçalo, J.; Waerenborgh, J. C.; Marques, N.; Pires De Matos, A. The "dissolution" of Europium and Ytterbium in Alcohols. *J. Alloys Compd.* **1998**, *275–277*, 841–843. https://doi.org/10.1016/S0925-8388(98)00454-X.

(55) Shannon, R. D. Revised Effective Ionic Radii and Systematic Studies of Interatomie Distances in Halides and Chaleogenides. *Acta Cryst* **1976**, *A32*, 751–767.

(56) Tsur, Y.; Dunbar, T. D.; Randall, C. A. Crystal and Defect Chemistry of Rare Earth Cations in $BaTiO_3$. *J. Electroceramics* **2001**, *7* (1), 25–34. https://doi.org/10.1023/A:1012218826733.

(57) Jankowska-Sumara, I.; Sitko, D.; Podgórna, M.; Pilch, M. The Electromechanical Behavior of Europium Doped $BaTiO_3$. *J. Alloys Compd.* **2017**, *724*, 703–710. https://doi.org/10.1016/j.jallcom.2017.07.090.

(58) Jiang, C.; Fang, L.; Shen, M.; Zheng, F.; Wu, X. Effects of Eu Substituting Positions and Concentrations on Luminescent, Dielectric, and Magnetic Properties of $SrTiO_3$ Ceramics. *Appl. Phys. Lett.* **2009**, *94* (7), 1–4. https://doi.org/10.1063/1.3082097.

(59) Fuentes, S.; Barraza, N.; Veloso, E.; Villarroel, R.; Llanos, J. Effects of Eu Substitution on Luminescent and Magnetic Properties of $BaTiO_3$ Nanomaterials. *J. Alloys Compd.* **2013**, *569*, 52–57. https://doi.org/10.1016/j.jallcom.2013.02.127.

(60) Jang, H. W.; Felker, D. A.; Bark, C. W.; Wang, Y.; Niranjan, M. K.; Nelson, C. T.; Zhang, Y.; Su, D.; Folkman, C. M.; Baek, S. H.; Lee, S.; Janicka, K.; Zhu, Y.; Pan, X. Q.; Fong, D. D.; Tsymbal, E. Y.; Rzchowski, M. S.; Eom, C. B. Metallic and Insulating Oxide Interfaces Controlled by Electronic Correlations. *Science (80-.).* **2011**, *331* (6019), 886–889. https://doi.org/10.1126/science.1198781.

(61) Varignon, J.; Bibes, M.; Zunger, A. Origin of Band Gaps in 3d Perovskite Oxides. *Nat. Commun.* **2019**, *10* (1), 1–11. https://doi.org/10.1038/s41467-019-09698-6.

(62) Bocquet, A. E.; Mizokawa, T.; Morikawa, K.; Fujimori, A.; Barman, S. R.; Maiti, K.;

Sarma, D. D.; Tokura, Y.; Onoda, M. Electronic Structure of Early 3d-Transition-Metal Oxides by Analysis of the 2p Core-Level Photoemission Spectra. *Phys. Rev. B* **1996**, *53* (3), 1161–1170.

(63) Brinker C.J., S. G. W. *Sol-Gel Science: The Physics and Chemistry of Sol-Gel Processing*; Elsevier Inc., 2013. https://doi.org/https://doi.org/10.1016/C2009-0-22386-5.

(64) Nawanil, C.; Panprom, P.; Makcharoen, W.; Khaosa-Ard, K.; Maluangnont, T.; Vittayakorn, W.; Vittayakorn, N. Synthesis of $BaTiO_3$@TiO_2-Sheet Core-Shell Structured Nanocomposites. *Integr. Ferroelectr.* **2019**, *195* (1), 196–207. https://doi.org/10.1080/10584587.2019.1570033.

(65) Zákutná, D.; NiŽňanský, D.; Barnsley, L. C.; Babcock, E.; Salhi, Z.; Feoktystov, A.; Honecker, D.; Disch, S. Field Dependence of Magnetic Disorder in Nanoparticles. *Phys. Rev. X* **2020**, *10* (3), 1–17. https://doi.org/10.1103/PhysRevX.10.031019.

(66) Pearsall, F.; Farahmand, N.; Lombardi, J.; Dehipawala, S.; Gai, Z.; O'Brien, S. Structure–Property Trends in a Hollandite Multiferroic by Fe Doping: Structural, Magnetic and Dielectric Characterization of Nanocrystalline $BaMn_{3-x}Fe_xTi_4O_{14+\delta}$. *J. Mater. Chem. C* **2020**, *8*, 7916–7927. https://doi.org/10.1039/d0tc00703j.

(67) Huang, L.; Liu, S.; Van Tassell, B. J.; Liu, X.; Byro, A.; Zhang, H.; Leland, E. S.; Akins, D. L.; Steingart, D. A.; Li, J.; O'Brien, S.; Tassell, B. J. Van; Liu, X.; Byro, A.; Zhang, H.; Leland, E. S.; Akins, D. L.; Steingart, D. A.; Li, J.; O'Brien, S. Structure and Performance of Dielectric Films Based on Self-Assembled Nanocrystals with a High Dielectric Constant. *Nanotechnology* **2013**, *24*, 415602. https://doi.org/10.1088/0957-4484/24/49/499601.

(68) Pearsall, F. A.; Lombardi, J.; O'Brien, S. Monomer Derived Poly(Furfuryl)/$BaTiO_3$ 0-3 Nanocomposite Capacitors: Maximization of the Effective Permittivity Through Control at the Interface. *ACS Appl. Mater. Interfaces* **2017**, *9* (46), 40324–40332. https://doi.org/10.1021/acsami.7b13879.

(69) Pearsall, F. A.; Lombardi, J.; Farahmand, N.; Tassel, B. van; Leland, E. S.; Huang, L.; Liu, S.; Yang, S.; Le, C.; Kymissis, I.; Kinget, P.; Sanders, S. R.; Steingart, D.; O'Brien, S. Polymer-Nanocrystal Nanocomposites: Device Concepts in Capacitors and Multiferroics. *IEEE Trans. Nanotechnol.* **2020**, *19*, 255–268.

(70) Yang, S.; Kymissis, I.; Leland, E. S.; Liu, S.; O'Brien, S. Influence of Electromigration on

the Maximum Operating Field of (Ba, Sr) TiO3/Parylene-C Composite Capacitors. *J. Vac. Sci. Technol. B* **2013**, *31* (6), 60603.

(71) Yang, S.; Tull, B. R.; Pervez, N. K.; Huang, L.; Leland, E. S.; Steigart, D. A.; O'Brien, S.; Kymissis, I. Asymmetric Leakage in (Ba, Sr)TiO_3 Nanoparticle/Parylene-C Composite Capacitors. *J. Polym. Sci. Part B Polym. Phys.* **2013**, *51* (1), 35–38. https://doi.org/10.1002/polb.23156.

(72) Teverovsky, A. Breakdown Voltages in Ceramic Capacitors with Cracks. *IEEE Trans. Dielectr. Electr. Insul.* **2012**, *19* (4), 1448–1455. https://doi.org/10.1109/TDEI.2012.6260022.

(73) Ribeiro, W. C.; Joanni, E.; Savu, R.; Bueno, P. R. Nanoscale Effects and Polaronic Relaxation in $CaCu_3Ti_4O_{12}$ Compounds. *Solid State Commun.* **2011**, *151* (2), 173–176. https://doi.org/10.1016/j.ssc.2010.10.034.

(74) Sihvola, A. H.; Institution of, E. E. *Electromagnetic Mixing Formulas and Applications*; Electromagnetics and Radar Series; Institution of Electrical Engineers, 1999.

(75) Lunkenheimer, P.; Götzfried, T.; Fichtl, R.; Weber, S.; Rudolf, T.; Loidl, A.; Reller, A.; Ebbinghaus, S. G. Apparent Giant Dielectric Constants, Dielectric Relaxation, and Ac-Conductivity of Hexagonal Perovskites $La_{1.2}Sr_{2.7}BO_{7.33}$ (B=Ru, Ir). *J. Solid State Chem.* **2006**, *179* (12), 3965–3973. https://doi.org/10.1016/j.jssc.2006.09.005.

(76) Adams, T. B.; Sinclair, D. C.; West, A. R. Giant Barrier Layer Capacitance Effects in $CaCu_3Ti_4O_{12}$ Ceramics. *Adv. Mater.* **2002**, *14* (18), 1321–1323.

(77) Kuang, X.; Bridges, C.; Allix, M.; Claridge, J. B.; Hughes, H.; Rosseinsky, M. J. Internal Barrier Layer Capacitance Effect in Hexagonal Perovskite $Ba_4YMn_3O_{11.5}$ Ceramics. *Chem. Mater.* **2006**, *18* (21), 5130–5136. https://doi.org/10.1021/cm0612752.

(78) Greczynski, G.; Hultman, L. Compromising Science by Ignorant Instrument Calibration—Need to Revisit Half a Century of Published XPS Data. *Angew. Chemie - Int. Ed.* **2020**, *59* (13), 5002–5006. https://doi.org/10.1002/anie.201916000.

(79) Guo, Z.; Yang, L.; Qiu, H.; Zhan, X.; Yin, J.; Cao, L. Structural, Magnetic and Dielectric Properties of Fe-Doped $BaTiO_3$ Solids. *Mod. Phys. Lett. B* **2012**, *26* (09), 1250056. https://doi.org/10.1142/S021798491250056X.

(80) Hudson, L. T.; Kurtz, R. L.; Robey, S. W.; Temple, D.; Stockbauer, R. L. Photoelectron Spectroscopic Study of the Valence and Core-Level Electronic Structure of $BaTiO_3$. *Phys.*

Rev. B **1993**, *47* (3), 1174–1180. https://doi.org/10.1103/PhysRevB.47.1174.

(81) Ehre, D.; Cohen, H.; Lyahovitskaya, V.; Lubomirsky, I. X-Ray Photoelectron Spectroscopy of Amorphous and Quasiamorphous Phases of $BaTiO_3$ and $SrTiO_3$. *Phys. Rev. B - Condens. Matter Mater. Phys.* **2008**, *77* (18), 1–6. https://doi.org/10.1103/PhysRevB.77.184106.

(82) Erdem, B.; Hunsicker, R. A.; Simmons, G. W.; David Sudol, E.; Dimonie, V. L.; El-Aasser, M. S. XPS and FTIR Surface Characterization of TiO_2 Particles Used in Polymer Encapsulation. *Langmuir* **2001**, *17* (9), 2664–2669. https://doi.org/10.1021/la0015213.

(83) Kim, D.; Jin, Y. H.; Jeon, K. W.; Kim, S.; Kim, S. J.; Han, O. H.; Seo, D. K.; Park, J. C. Blue-Silica by Eu2+-Activator Occupied in Interstitial Sites. *RSC Adv.* **2015**, *5* (91), 74790–74801. https://doi.org/10.1039/c5ra15641f.

(84) Mariscal, A.; Quesada, A.; Martín-Luengo, A. T.; García, M. Á.; Bonanni, A.; Fernández, J.; Serna, R. Highly Oriented EuO Nanocrystalline Films via Reduction Process - NIR Optical Response. *ArXiv* **2017**, 1–22.

(85) Li, W.; Zhao, R.; Wang, L.; Tang, R.; Zhu, Y.; Lee, J. H.; Cao, H.; Cai, T.; Guo, H.; Wang, C.; Ling, L.; Pi, L.; Jin, K.; Zhang, Y.; Wang, H.; Wang, Y.; Ju, S.; Yang, H. Oxygen-Vacancy-Induced Antiferromagnetism to Ferromagnetism Transformation in $Eu_{0.5}Ba_{0.5}TiO_{3-\delta}$ Multiferroic Thin Films. *Sci. Rep.* **2013**, *3* (September 2014), 0–6. https://doi.org/10.1038/srep02618.

(86) Abbate, M.; De Groot, F. M. F.; Fuggle, J. C.; Fujimori, A.; Tokura, Y.; Fujishima, Y.; Strebel, O.; Domke, M.; Kaindl, G.; Van Elp, J.; Thole, B. T.; Sawatzky, G. A.; Sacchi, M.; Tsuda, N. Soft-X-Ray-Absorption Studies of the Location of Extra Charges Induced by Substitution in Controlled-Valence Materials. *Phys. Rev. B* **1991**, *44* (11), 5419–5422. https://doi.org/10.1103/PhysRevB.44.5419.

(87) Nakayama, M.; Usui, T.; Uchimoto, Y.; Wakihara, M.; Yamamoto, M. Changes in Electronic Structure upon Lithium Insertion into the A-Site Deficient Perovskite Type Oxides $(Li,La)TiO_3$. *J. Phys. Chem. B* **2005**, *109* (9), 4135–4143. https://doi.org/10.1021/jp046062j.

(88) Laskowski, R.; Blaha, P. Understanding the L2,3 X-Ray Absorption Spectra of Early 3d Transition Elements. *Phys. Rev. B - Condens. Matter Mater. Phys.* **2010**, *82* (20), 1–6. https://doi.org/10.1103/PhysRevB.82.205104.

(89) Ohtomo, A.; Muller, D. A.; Grazul, J. L.; Hwang, H. Y. Artificial Charge-Modulation in Atomic-Scale Perovskite Titanate Superlattices. *Nature* **2002**, *419* (6905), 378–380. https://doi.org/10.1038/nature00977.

(90) Iori, F.; Gatti, M.; Rubio, A. Role of Nonlocal Exchange in the Electronic Structure of Correlated Oxides. *Phys. Rev. B - Condens. Matter Mater. Phys.* **2012**, *85* (11), 1–10. https://doi.org/10.1103/PhysRevB.85.115129.

(91) Rahimi, N.; Pax, R. A.; Gray, E. M. A. Review of Functional Titanium Oxides. I: TiO_2 and Its Modifications. *Prog. Solid State Chem.* **2016**, *44* (3), 86–105. https://doi.org/10.1016/j.progsolidstchem.2016.07.002.

(92) Giannakoudakis, D. A.; Pearsall, F.; Florent, M.; Lombardi, J.; O'Brien, S.; Bandosz, T. J. Barium Titanate Perovskite Nanoparticles as a Photoreactive Medium for Chemical Warfare Agent Detoxification. *J. Colloid Interface Sci.* **2018**, *531*, 233–244. https://doi.org/10.1016/j.jcis.2018.07.053.

(93) Royer, S.; Duprez, D.; Can, F.; Courtois, X.; Batiot-Dupeyrat, C.; Laassiri, S.; Alamdari, H. Perovskites as Substitutes of Noble Metals for Heterogeneous Catalysis: Dream or Reality. *Chem. Rev.* **2014**, *114* (20), 10292–10368. https://doi.org/10.1021/cr500032a.

(94) Lin, Y. C.; Hohn, K. L. Perovskite Catalysts-A Special Issue on Versatile Oxide Catalysts. *Catalysts* **2014**, *4* (3), 305–306. https://doi.org/10.3390/catal4030305.

(95) Zheng, S. Y.; Chiou, J. W.; Li, Y. H.; Yang, C. F.; Ray, S. C.; Chen, K. H.; Chang, C. Y.; Shelke, A. R.; Wang, H. T.; Yeh, P. H.; Lai, C. Y.; Hsieh, S. H.; Pao, C. W.; Chen, J. L.; Lee, J. F.; Tsai, H. M.; Fu, H. W.; Hua, C. Y.; Lin, H. J.; Chen, C. Te; Pong, W. F. Correlation among Photoluminescence and the Electronic and Atomic Structures of Sr_2SiO_4:XEu^{3+} Phosphors: X-Ray Absorption and Emission Studies. *Sci. Rep.* **2020**, *10* (1), 1–12. https://doi.org/10.1038/s41598-020-69428-7.

(96) Zhang, J.; Hao, Y.; Bi, M.; Dong, G.; Liu, X.; Bi, K. Outstanding Photoluminescence in Pr^{3+}-Doped Perovskite Ceramics. *Micromachines* **2018**, *9*, 419.

(97) Yang, L.; Kruse, B. Revised Kubelka--Munk Theory. I. Theory and Application. *J. Opt. Soc. Am. A* **2004**, *21* (10), 1933–1941. https://doi.org/10.1364/JOSAA.21.001933.

(98) Maneeshya, L. V.; Lekshmy, S. S.; Thomas, P. V.; Joy, K. Europium Incorporated Barium Titanate Thin Films for Optical Applications. *J. Mater. Sci. Mater. Electron.* **2014**, *25* (6), 2507–2515. https://doi.org/10.1007/s10854-014-1903-5.

(99) Doat, A.; Pellé, F.; Gardant, N.; Lebugle, A. Synthesis of Luminescent Bioapatite Nanoparticles for Utilization as a Biological Probe. *J. Solid State Chem.* **2004**, *177* (4–5), 1179–1187. https://doi.org/10.1016/j.jssc.2003.10.023.

(100) Guo, Y.; Moon, B. K.; Choi, B. C.; Jeong, J. H.; Kim, J. H.; Choi, H. Fluorescence Properties with Red-Shift of Eu^{2+} Emission in Novel Phosphor-Silicate Apatite $Sr_3LaNa(PO_4)_2SiO_4$ Phosphors. *Ceram. Int.* **2016**, *42* (16), 18324–18332. https://doi.org/10.1016/j.ceramint.2016.08.163.

(101) Benkstein, K. D.; Montgomery, C. B.; Vaudin, M. D.; Semancik, S. Mater. Res. Soc. Symp. Proc. Vol. 828 © 2005 Materials Research Society A7.4.1. **2005**, *828*, 1–6.

(102) Binnemans, K.; Moors, D. Narrow Band Photoluminescence of Europium-Doped Liquid Crystals. *J. Mater. Chem.* **2002**, *12* (12), 3374–3376. https://doi.org/10.1039/b206810a.

(103) Baran, A.; Barzowska, J.; Grinberg, M.; Mahlik, S.; Szczodrowski, K.; Zorenko, Y. Binding Energies of Eu^{2+} and Eu^{3+} Ions in β-Ca_2SiO_4 Doped with Europium. *Opt. Mater. (Amst).* **2013**, *35* (12), 2107–2114. https://doi.org/10.1016/j.optmat.2013.05.030.

(104) Xie, H.; Lu, J.; Guan, Y.; Huang, Y.; Wei, D.; Seo, H. J. Abnormal Reduction, $Eu^{3+} \rightarrow Eu^{2+}$, and Defect Centers in Eu^{3+}-Doped Pollucite, $CsAlSi_2O_6$, Prepared in an Oxidizing Atmosphere. *Inorg. Chem.* **2014**, *53* (2), 827–834. https://doi.org/10.1021/ic402169w.

(105) Baran, A.; Mahlik, S.; Grinberg, M.; Cai, P.; Kim, S. I.; Seo, H. J. Luminescence Properties of Different Eu Sites in $LiMgPO_4$:Eu^{2+}, Eu^{3+}. *J. Phys. Condens. Matter* **2014**, *26* (38). https://doi.org/10.1088/0953-8984/26/38/385401.

(106) Ai, K.; Zhang, B.; Lu, L. Europium-Based Fluorescence Nanoparticle Sensor for Rapid and Ultrasensitive Detection of an Anthrax Biomarker. *Angew. Chem. Int. Ed. Engl.* **2009**, *48* (2), 304–308. https://doi.org/10.1002/anie.200804231.

(107) Peng, H.; Stich, M. I. J.; Yu, J.; Sun, L.-N.; Fischer, L. H.; Wolfbeis, O. S. Luminescent Europium(III) Nanoparticles for Sensing and Imaging of Temperature in the Physiological Range. *Adv. Mater.* **2010**, *22* (6), 716–719. https://doi.org/10.1002/adma.200901614.

(108) Yang, P.; Quan, Z.; Li, C.; Kang, X.; Lian, H.; Lin, J. Bioactive, Luminescent and Mesoporous Europium-Doped Hydroxyapatite as a Drug Carrier. *Biomaterials* **2008**, *29* (32), 4341–4347. https://doi.org/10.1016/j.biomaterials.2008.07.042.

(109) Picot, A.; D'Aléo, A.; Baldeck, P. L.; Grichine, A.; Duperray, A.; Andraud, C.; Maury, O.

Long-Lived Two-Photon Excited Luminescence of Water-Soluble Europium Complex: Applications in Biological Imaging Using Two-Photon Scanning Microscopy. *J. Am. Chem. Soc.* **2008**, *130* (5), 1532–1533. https://doi.org/10.1021/ja076837c.

(110) Upputuri, P. K.; Pramanik, M. Photoacoustic Imaging in the Second Near-Infrared Window: A Review. *J. Biomed. Opt.* **2019**, *24* (4), 40901.

(111) Pratt, E. C.; Shaffer, T. M.; Zhang, Q.; Drain, C. M.; Grimm, J. Nanoparticles as Multimodal Photon Transducers of Ionizing Radiation. *Nat. Nanotechnol.* **2018**, *13* (5), 418–426.

(112) Huang, R. H.; Sobol, N. B.; Younes, A.; Mamun, T.; Lewis, J. S.; Ulijn, R. V; O'Brien, S. P. Comparison of Methods for Surface Modification of Barium Titanate Nanoparticles for Aqueous Dispersibility: Towards Biomedical Utilization of Perovskite Oxides. *ACS Appl. Mater. Interfaces* **2020**. https://doi.org/10.1021/acsami.0c10063.